

THESIS FOR THE DEGREE OF LICENTIATE OF ENGINEERING

Antenna Design, Radiobiological Modelling, and
Non-invasive Monitoring for Microwave
Hyperthermia

MORTEZA GHADERI ARAM



CHALMERS
UNIVERSITY OF TECHNOLOGY

Department of Electrical Engineering
Chalmers University of Technology
Gothenburg, Sweden, 2022

Antenna Design, Radiobiological Modelling, and Non-invasive Monitoring for Microwave Hyperthermia

MORTEZA GHADERI ARAM

Copyright © 2022 MORTEZA GHADERI ARAM
All rights reserved.

Technical Report No. 1111-111X
ISSN 3.1415-9265
This thesis has been prepared using L^AT_EX.

Department of Electrical Engineering
Chalmers University of Technology
SE-412 96 Gothenburg, Sweden
Phone: +46 (0)31 772 1000
www.chalmers.se

Printed by Chalmers Reproservice
Gothenburg, Sweden, February 2022

To my family.

Abstract

The death toll of cancers is on the rise worldwide and surviving patients suffer significant side effects from conventional therapies. To reduce the level of toxicity in patients treated with the conventional treatment modalities, hyperthermia (HT) has been investigated as an adjuvant modality and shown to be a potent tumor cell sensitizer for radio- and chemotherapy. During the past couple of decades, several clinical radiofrequency HT systems, aka applicators, have been developed to heat tumors. Systems based on radiative applicators are the most widely used within the hyperthermic community. They consist of a conformal antenna array and need a beamforming method in order to focus EM energy on the tumor through constructive interference while sparing the healthy tissue from excessive heating. Therefore, a hyperthermia treatment planning (HTP) stage is required before each patient's first treatment session to optimize and control the EM power deposition as well as the resultant temperature distribution.

Despite the vast amount of effort invested in HTP and the progress made in this regard during recent years, the clinical exploitation of HT is still hampered by technical limitations and patients can still experience discomfort during clinical trials. This, therefore, calls for a more efficient hardware design, better control of EM power deposition to minimize unwanted hotspots, and more accurate quantification and monitoring of the treatment outcome. Given these demands, the present report tries to address some of the above-mentioned challenges by proposing

- A new antenna model customized for HT applications which surpasses previously proposed models from several points of view.
- A hybrid beamforming method for faster convergence and a versatile, robust thermal solver for handling sophisticated scenarios.
- A radiobiological model to quantify the outcome of a combined treatment modality of the Gamma Knife radiosurgery and HT.
- A differential image reconstruction method to assess the feasibility of using the same system for both heating and microwave thermometry.

Keywords: Bio-Electromagnetics, UWB Antennas, Hyperthermia, Microwave Thermometry, Radiobiological Modeling.

List of Publications

This report is based on the following publications:

[A] **Morteza Ghaderi Aram**, Hadi Aliakbarian, Hana Dobšíček Trefná, “An ultra-wideband compact design for hyperthermia: Open ridged-waveguide antenna”. Published in *IET Microwaves, Antennas & Propagation*, Jan. 2022.

[B] **Morteza Ghaderi Aram**, Hadi Aliakbarian, Hana Dobšíček Trefná, “A phased array applicator based on open ridged-waveguide antenna for microwave hyperthermia”. Published in *Microwave and Optical Technology Letters*, Sep. 2021.

[C] **Morteza Ghaderi Aram**, Massimiliano Zanoli, Håkan Nordström, Iuliana Toma-Dasu, Klas Blomgren, Hana Dobšíček Trefná, “Radiobiological Evaluation of Combined Gamma Knife Radiosurgery and Hyperthermia for Pediatric Neuro-Oncology”. Published in *Cancers*, Jun. 2021.

[D] **Morteza Ghaderi Aram**, Larisa Beilina, Hana Dobšíček Trefná, “Microwave thermometry with potential application in non-invasive monitoring of hyperthermia”. Published in *Journal of Inverse and Ill-posed Problems*, Oct. 2020.

Other publications by the author, not included in this report, are:

[E] B. Elling, **M. G. Aram**, S. Liacer, H. D. Trefná, “The UWB phased array applicator: novel cooling solutions”. *33rd Annual Meeting of the European Society for Hyperthermic Oncology (ESHO)*, Warsaw, Poland, May 2019.

[F] **M. G. Aram**, H. Nordström, I. Toma-Dasu, K. Blomgren, H. D. Trefná, “Radiobiological modeling of hyperthermia combined with Gamma Knife radiosurgery in pediatric brain cancer”. *13th International Congress of Hyperthermic Oncology (ICHO)*, Digital, Oct. 2021.

[G] L. Beilina, **M. G. Aram**, E. M. Karchevskii, “An adaptive finite element method for solving 3D electromagnetic volume integral equation with applications in microwave thermometry”. *Submitted to Journal of Computational Physics*, Elsevier, Nov. 2021.

Acknowledgments

Looking back, I thank you dear God for all the blessings. Looking forward, I trust you more than ever.

For all those whose time and energies played a role in helping me get to this stage of my academic career, I am forever grateful. A special shout-out goes to all my friends at Chalmers who are fortunately too many to mention here one by one. I am so very thankful for the moments we shared and all the lessons we learned together.

Acronyms

PLD:	Power Loss Density
SAR:	Specific Absorption Rate
HT:	Hyperthermia
HTP:	Hyperthermia Treatment Planning
ORWG:	Open Ridged-Waveguide
CEM:	Computational Electromagnetics
FEM:	Finite Element Method
FDTD:	Finite Difference Time Domain
CAD:	Computer Aided Design
RT:	Radiotherapy
GTV:	Gross Tumor Volume
TCP:	Tumor Control Probability

Contents

Abstract	i
List of Papers	iii
Acknowledgements	v
Acronyms	v
I Overview	1
1 Introduction	3
1.1 Human Head Cancers	4
1.2 Hyperthermia	7
1.3 Fundamentals of RF/MW HT	9
EM Fields & Electrical Properties	9
Power Absorption	10
Heat Transfer Model	11
1.4 HT Treatment and Systems	12
Superficial Hyperthermia	13
Deep Hyperthermia	14
Whole-body Hyperthermia	16

1.5	Outline of the Thesis	16
2	Antenna Design	19
2.1	Design Criteria for HT Antennas	20
2.2	The ORWG Model	22
2.3	Hydrogel Bolus and Phantom Preparation	24
2.4	Measurement & Verification	25
2.5	Phased Array Applicator	27
3	Hyperthermia Treatment Planning	33
3.1	Step I. Human Models for CEM Research	35
3.2	Step II. EM Simulation & Optimization	37
	EM Field Simulation	37
	SAR-based Optimization	39
3.3	Step III. Thermal Simulation	41
	Development of a FEniCS-based Thermal Solver	43
	Thermal Evaluation & Analysis	46
3.4	Radiobiological Modelling	48
	Radiosurgery with Leksell Gamma Knife	49
	Radiobiology	50
	LQ Model	50
	Hypoxia	51
	Thermoradiotherapy	52
4	Microwave Thermometry	57
4.1	The Reconstruction Algorithm	58
	Least-Square Reconstruction	59
	Adaptive FEM Refinement	59
4.2	Proof of Concept – Measurement	60
	Monopole System	60
5	Summary of included papers	65
5.1	Paper A	65
5.2	Paper B	66
5.3	Paper C	67
5.4	Paper D	68
6	Concluding Remarks	71

References	73
II Papers	91
A An ultra-wideband compact design for hyperthermia: Open ridged-waveguide antenna	A1
B A phased array applicator based on open ridged-waveguide antenna for microwave hyperthermia	B1
C Radiobiological evaluation of combined Gamma Knife radiosurgery and hyperthermia for pediatric neuro-oncology	C1
D Microwave thermometry with potential application in non-invasive monitoring of hyperthermia	D1

Part I

Overview

CHAPTER 1

Introduction

Cancer, the uncontrolled growth of abnormal cells in the body, is among the leading causes of death worldwide [1]. Cancers have been classified into 100 different types depending on the type of primary cell from which the uncontrolled growth starts. The cancerous cells can move and form malignant tumors which, if not diagnosed and treated timely, can further spread to other parts of the body through a process known as metastasis. This stage of the disease may lead to a serious and life-threatening condition [2].

Surgery, radiotherapy, and chemotherapy are the standard cancer treatment modalities that can be used alone or in combination with adjuvant methods. Tumor site and stage are the deciding factors in choosing the appropriate type of therapy. Surgery is the longest-standing therapy for cancer but cannot be performed for non-resectable tumors. Moreover, since the simple excision of tumors in some patients is not sufficient to prevent a relapse, surgery usually needs to be accompanied by other modalities to improve the tumor control probability. For radiotherapy (RT), there are limitations regarding the dose tolerance of critical organs. In many cases and particularly in recurrent tumors, these limitations on the admissible level of the dose can make RT treatments ineffective. RT can further lead to late complications and an increased

risk of developing secondary cancers. Utilizing one or more anti-cancer drugs, chemotherapy (CT) may eradicate cancer, but its efficacy varies largely depending on the type and stage of the cancer. CT exhibits its best performance if administered in the early stage of the disease when the metastasis is undetectable [3].

The remainder of this chapter presents the statistics of human head cancers, summarizes the biological aspects of microwave HT, and overviews the technology required to apply different types of HT.

1.1 Human Head Cancers

Human head cancers, usually classified separately into Head&Neck (H&N) and brain cancers, are one of the most common cancer categories worldwide [4]. Global incidence of H&N cancers, occurring in regions shown in Figure 1.1, has been estimated to be between 400 000 and 600 000 new cases each year, resulting in a mortality rate of between 223 000 and 300 000 deaths per year [5], [6]. Unfortunately, the number of patients dying from cancers in the regions of body reported in Table 1.1 is increasing each year. The table shows the cancer statistics in human head both globally and in Sweden while Figure 1.2 visualizes the percentage of each type of head cancer in 2020 [7]. The situation nationwide in Sweden is similar to the global cancer figures and according to the Swedish Head and Neck Cancer Register (SweHNCR), H&N cancer in Sweden constitutes 2.3% of all cancer incidences, comprising nine different sites reported in the table.

During the ten-year period of 2008-2017, SweHNCR reports 25% increase in the incidence of H&N cancer in Sweden by summarizing the number of cancer cases per diagnosis group in Figure 1.3. The relative 5-year survival rate for all patients with H&N cancer in the SweHNCR has been reported to be 67%, while the overall survival rate was 59% [9]. As can be seen from Figure 1.4, there are large differences in the relative survival rates between the different diagnosis groups, with hypopharyngeal patients having the lowest relative survival rate of 25%. Except lip patients, all the other categories have an average survival rate between 50 to 75%.

Despite all the advancements in the treatment of cancers in general, brain cancer management still remains challenging with a low chance of long-term survival. In many cases, Glioblastoma multiforme (GBM) is the most ag-

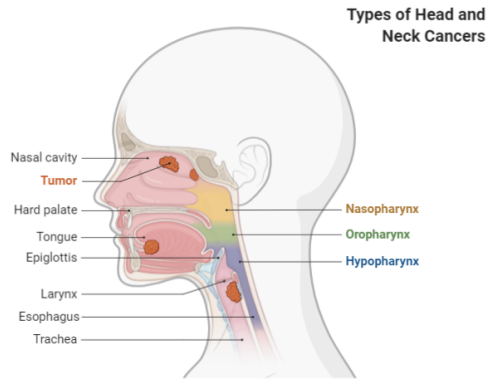


Figure 1.1: Head and neck cancer sites.

Table 1.1: Incidence, Mortality and Prevalence by cancer site in the head for all ages (Extracted from Globocan 2020 [8])

Cancer Sites	Worldwide			In Sweden		
	Number of New Cases	Number of Death	5-year prevalence	Number of New Cases	Number of Death	5-year prevalence
Esophagus	604 100	544 076	666 388	589	545	721
Thyroid	586 202	43 646	1 984 927	747	78	2 922
Lip, Oral Cavity	377 713	177 757	959 248	687	231	2 279
Brain, CNS	308 102	251 329	837 152	841	752	2 595
Larynx	184 615	99 840	518 380	154	64	561
Nasopharynx	133 354	80 008	382 507	31	7	113
Oropharynx	98 412	48 143	258 543	445	77	1 412
Hypopharynx	84 254	38 599	132 717	54	41	114
Salivary Glands	53 583	22 778	160 292	118	47	427
All Sites	2 430 335	1 306 176	—	3 666	1 842	—

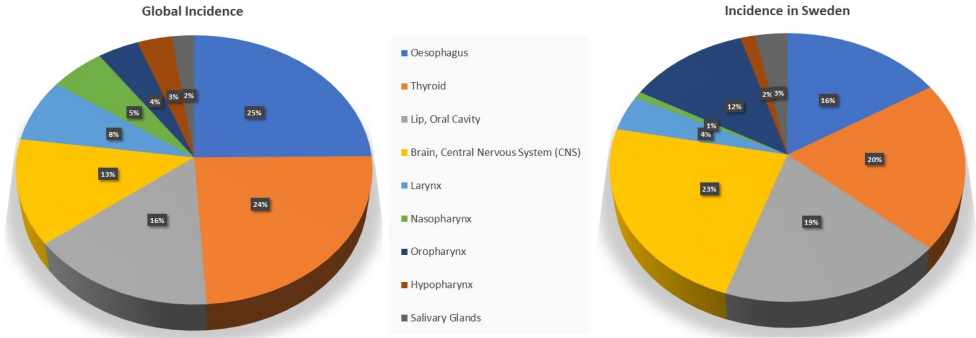


Figure 1.2: Incidence rate percentage of each type of cancer in human head based on Globocan Statistics in 2020.

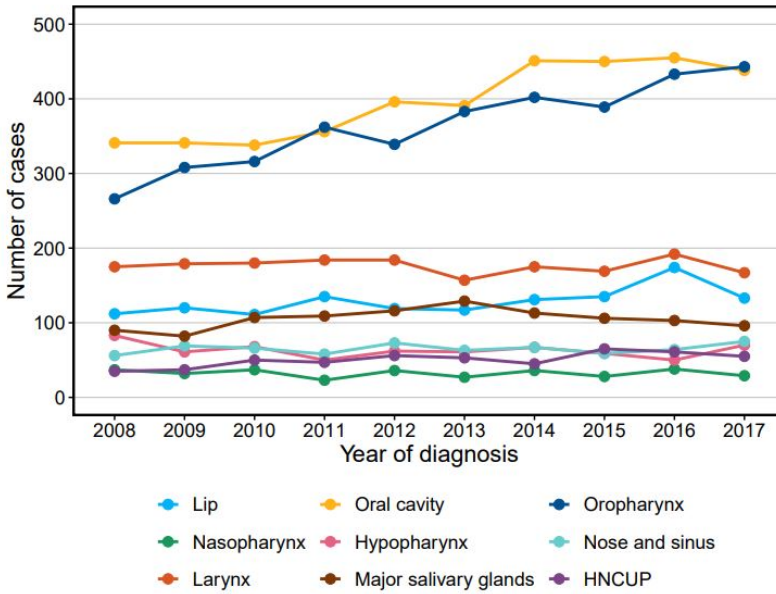


Figure 1.3: Number of cancer cases per diagnosis group during the years 2008-2017 in Sweden [9]

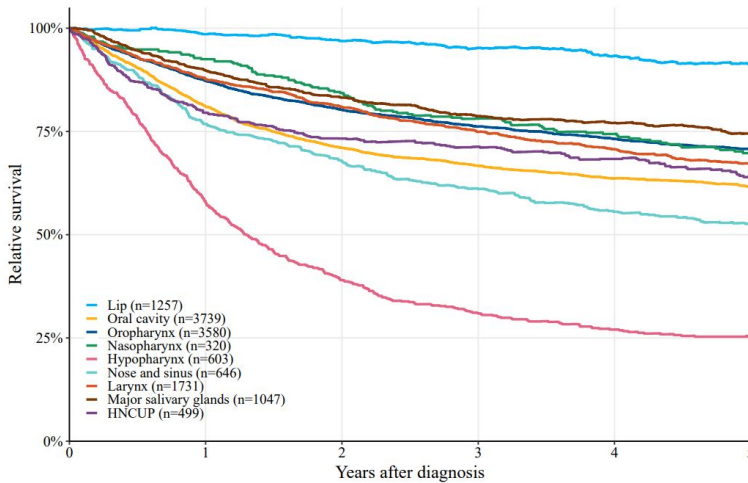


Figure 1.4: Five-year relative survival rates per diagnosis group in the SweHNCR, 2008-2017 [9]

gressive malignant type in adults with the tendency of a quick relapse after surgery. The average survival for patients with malignant gliomas is only 17 weeks which can be extended to 30 weeks after surgery and chemotherapy [10]. In children younger than 15 years old, brain tumors are the second most common cancer type, representing 20 – 30% of all childhood cancers. Medulloblastoma is the most common type in children for which treatments usually begin with surgical excision, followed by the addition of radiotherapy or chemotherapy to increase the disease-free survival rate. For these patients, overall survival reported in population-based studies [11] is roughly 50% to 60%. However, radiation often triggers late complications and severe side effects which is more consequential in children since even low doses of ionizing radiation to their brain can cause perturbed growth/ puberty [12], [13] as well as intellectual impairment [14].

1.2 Hyperthermia

Hyperthermia (HT) is a therapeutic modality that can be part of a multimodal oncological strategy when combined with radio- or chemotherapy. The aim of

HT is to raise tumor temperature to supraphysiological levels between 40°C and 44°C . Studies show that the mild increase in temperature enhances the concentration of oxygen in the tumor, therefore improving the effectiveness of radiotherapy [15], [16]. It also increases the blood flow in the heated area leading to increased perfusion which improves the drug absorption in cells for chemotherapy [17], [18].

The biological rationale for the use of hyperthermia is not completely understood. However, the proven mechanisms, as summarized in [19], include the inhibition of different DNA repair processes, direct/ indirect reduction of the hypoxic tumor cell fraction, increased perfusion and oxygen levels, and enhanced drug uptake. The clinically observed biological effects over HT temperature range are the following [20]. During HT, blood flow is increased by the tissue metabolism to counteract the temperature rise. When heated, the blood vessels in healthy tissues can vasodilate, to facilitate an increased blood flow. This process acts as a heat sink and reduces the temperature. In contrast to healthy tissues, tumorous tissues are far less capable of increasing the blood flow due to a chaotic vasculature which gives rise to regions suffering from improper perfusion and hypoxia. Therefore, the heat dissipation is slower in tumors and during HT heating their temperature tends to rise higher than the normal tissue does.

The addition of hyperthermia to the routine cancer therapies increases the tumor response rate by typically about 20% [21]. This happens while the radiation- or chemotherapy-related toxicity to the healthy tissue is not intensified because the effect of HT will be tumor-selective when heat delivery is confined to the tumor site [22]. Therefore, for the same therapeutic outcome without any reduction of the effect on the tumor, HT allows for a lower radio or cytotoxic dose which will eventually result in a lower risk of treatment-related side effects. For primary tumors, HT can be added to the full dose radiotherapy or chemotherapy treatment scheme to enhance tumor management. Efficacy of the method has been demonstrated through randomized trials for cervical, bladder, and H&N cancers as well as for soft tissue sarcomas [23]–[25]. In case of recurrence of a tumor after previous treatments where a higher risk of side effects is associated with re-treatments, the addition of HT can result in a good tumor control allowing for a lower level of dose with a minimal risk of side effects. Low dose re-irradiation combined with HT is a proven treatment method for recurrent breast cancer and recurrent malignant

melanoma [26], [27].

Electromagnetic (EM) radiation at either radiofrequency (RF) or microwave frequencies (MW) [28], [29] and the mechanical energy in form of ultrasound (US) [30], [31] are widely used in deep HT systems. This thesis focuses on microwave hyperthermia, while the readers interested to US-based systems may consult the relevant literature [32].

1.3 Fundamentals of RF/MW HT

Time-varying electric field \mathbf{E} (V/m) and magnetic intensity \mathbf{H} (A/m) are related to each other and to their sources, charge ρ (C/m³) and current density \mathbf{J} (A/m²), by Maxwell's set of equations [33]. Interaction of EM waves with lossy media such as biological tissues results in the Power Loss Density (PLD) deposition which eventually turns into heat. This section first presents a short overview on EM fields, their propagation, and the power deposition in biological tissues. It then concludes the discussion by reviewing a widely used thermal model for the heat transfer in perfused tissues.

EM Fields & Electrical Properties

Assuming a sinusoidal time dependency in Maxwell's equations, we can separate the temporal and spatial dependencies to work in the phasor domain as follows:

$$\nabla \times \overline{\mathbf{E}} = -j\omega\mu\overline{\mathbf{H}} \quad (1.1)$$

$$\nabla \times \overline{\mathbf{H}} = \overline{\mathbf{J}} + j\omega\epsilon\overline{\mathbf{E}} \quad (1.2)$$

$$\nabla \cdot \overline{\mathbf{D}} = \rho \quad (1.3)$$

$$\nabla \cdot \overline{\mathbf{B}} = 0 \quad (1.4)$$

where

$$\begin{aligned}\mathbf{E}(x, y, z; t) &= \text{Re}\{\overline{\mathbf{E}} e^{j\omega t}\} \\ \mathbf{H}(x, y, z; t) &= \text{Re}\{\overline{\mathbf{H}} e^{j\omega t}\} \\ \mathbf{J}(x, y, z; t) &= \text{Re}\{\overline{\mathbf{J}} e^{j\omega t}\} \\ \overline{\mathbf{D}} &= \epsilon \overline{\mathbf{E}}, \quad \overline{\mathbf{B}} = \mu \overline{\mathbf{H}}.\end{aligned}$$

Since the interaction between \mathbf{B} fields and biological materials through magnetization is insignificant, we can consider only two mechanisms of the interaction with \mathbf{E} fields through which currents are produced in tissues. The first mechanism is the drift of free conduction charges in the material in response to the applied \mathbf{E} field. This conduction current is $\sigma \mathbf{E}$, where σ (S/m) is the conductivity. The second mechanism is dielectric polarization, which may arise when the positive and negative charges of a molecule are displaced slightly from their equilibrium positions due to the applied \mathbf{E} field, hence the name displacement current. This effect is taken into account in a dimensionless quantity known as electric susceptibility, χ . Now, it is useful to define the complex permittivity of the material as follows

$$\epsilon = \epsilon_0 \left(1 + \chi + \frac{\sigma}{j\omega\epsilon_0} \right) = \epsilon_0 (\epsilon' - j\epsilon''). \quad (1.5)$$

The additional polarization charge is accounted for by ϵ' whilst the effect of the conduction of free charges is described by ϵ'' . The parameter ϵ'' determines how much power is absorbed from the electric field. A related parameter often used in the literature is loss tangent $\tan\delta = \frac{\epsilon''}{\epsilon'}$. Notice that in biological tissues, both ϵ' and ϵ'' vary with the frequency of the applied field and therefore are considered as dispersive. Debye and Cole-Cole dispersion models that represent the dielectric spectra of tissues are discussed by Gabriel et al. [34].

Power Absorption

The following discussion is to show in the HT context how we derive the amount of the power dissipated in a volume V from the amount of the power entering that volume enclosed by surface S . According to Poynting theorem [33], energy exchange in a source-free volume V satisfies the following equilibrium

$$\int_V \mathbf{E} \cdot \mathbf{J} \, dv = -\frac{d}{dt} (W_E + W_H) - \oint_S \mathbf{E} \times \mathbf{H} \cdot d\mathbf{s} \quad (1.6)$$

In other words, the rate of energy change in volume V can be determined by the change of electrically (W_E) and magnetically (W_H) stored energy in that volume as well as the amount of energy flux passing through the enclosing surface S of the same volume. Since there are no stored energy in the patients body and in biological tissues in general, the first term in the right-hand side of Equation 1.6 can be safely omitted. From a measurement point of view, time-averaged quantities are more useful than the instantaneous quantities in Equation 1.6, and from phasor domain relations, we know that $\langle \mathbf{E} \times \mathbf{H} \rangle_T = \frac{1}{2} \text{Re}\{\overline{\mathbf{E}} \times \overline{\mathbf{H}}^*\}$ where \mathbf{H}^* is the complex conjugate of \mathbf{H} . Thus, we get

$$\frac{1}{2} \int_V \text{Re}\{\overline{\mathbf{E}} \cdot \overline{\mathbf{J}}^*\} \, dv = -\frac{1}{2} \oint_S \text{Re}\{\overline{\mathbf{E}} \times \overline{\mathbf{H}}^*\} \cdot d\mathbf{s} \quad (1.7)$$

Since $\mathbf{J} = \sigma \mathbf{E}$, the left-hand side of the Equation 1.7 represents heat-producing Ohmic losses. In mathematical terms, the incremental energy (dW) absorbed by (dissipated in) an elemental volume (dv) is $P = \frac{dW}{dv} = \frac{1}{2} \sigma |\mathbf{E}|^2$. Equation 1.7 shows that the time-averaged power dissipated in V is equal to the time-averaged power passing into V through the surface S .

The specific absorption rate (SAR), i.e. mass normalized energy absorption rate, is defined as the time derivative of the incremental energy absorbed by an incremental mass (dm) contained in dv of a given density (ρ) as follows

$$SAR = \frac{d}{dt} \left[\frac{dW}{dm} \right] = \frac{d}{dt} \left[\frac{dW}{\rho dv} \right] = \frac{d}{dt} \left[\frac{1}{\rho} P \right] = \frac{\sigma}{2\rho} |\mathbf{E}|^2 \quad (1.8)$$

The unit for SAR is W/kg .

Heat Transfer Model

The deposited EM energy, discussed in the previous section, eventually turns into heat due to Joule heating. A simplified version of the heat equation in homogeneous, non-perfused media is usually used to relate the SAR to incremental change in temperature ($\frac{\Delta T}{\Delta t}$) as follows

$$SAR = c \frac{\Delta T}{\Delta t} \quad (1.9)$$

where c is the heat capacity ($J/^\circ C/kg$).

Equation 1.9 gives only an estimate of how the temperature may evolve in the tissue during the SAR deposition. Biological models, however, involve perfused tissues due to blood circulation in body, and this fact is not accounted for in this simple formula. The most established way to model this phenomenon while taking into account the blood perfusion rate is by using the Pennes Bioheat equation [35] as follows:

$$c\rho\frac{\partial T}{\partial t} = \nabla \cdot (\kappa\nabla T) + PLD - c_b\omega_b(T - T_b) \quad (1.10)$$

where T ($^\circ C$) is temperature; ρ (kg/m^3) is mass density; κ ($W/^\circ C/m$) is thermal conductivity; and T_b , c_b , ω_b ($kg/m^3/s$) are temperature, heat capacity, and perfusion rate of blood, respectively.

1.4 HT Treatment and Systems

Radiative applicators use EM energy mostly in the RF or microwave range to deliver heat into the target/ body. They can be categorized into two types: internal and external. Internal heating includes interstitial heat delivery through the insertion of tiny antennas into tumor. External heating of deep-seated tumors involves use of a conformal multi-element antenna phased array used to emit microwaves or radiowaves in order to transfer the EM energy into the tissue. External heating techniques require a Water Bolus (WB) to be placed between the applicator and the body. The presence of WB improves the impedance match to the tissue, reduces the level of stray radiation compared with the case of an air gap between applicator and tissue, and provides cooling for the skin and other superficial tissues. WB also spaces the tissue from the relatively rapidly decaying near-field, or in other words, it helps to avoid putting the patient's body in the reactive near-field by setting it instead within or beyond the radiating near-field zone (Fresnel region) [36].

The general configuration of an RF/ microwave HT system is given in Figure 1.5. Four main parts to such a system can be identified from the figure as follows: (1) an antenna applicator which also includes water bolus and the cooling system (2) a power amplification unit (3) the control and treatment planning unit and (4) a thermometry feedback loop. All the parts besides the amplifier unit will be discussed in the following chapters. For a thorough dis-

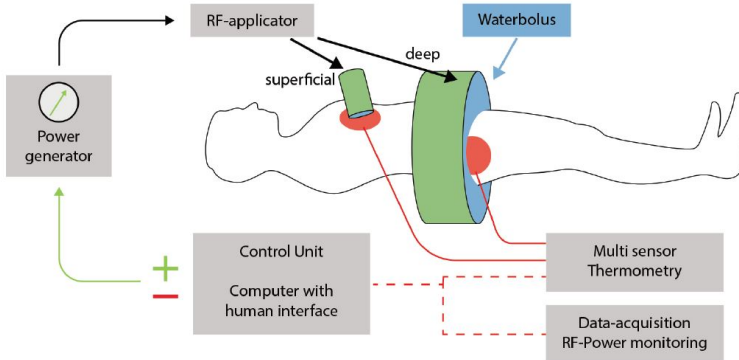


Figure 1.5: Conceptual schema of a typical HT system (Taken and reprinted from [43])

cussion about HT amplifier systems and the hardware design of such systems, interested readers can consult [37], [38]. Thermometry is still accomplished invasively through the insertion of temperature sensors into body. A non-invasive alternative for temperature measurement, not shown in Figure 1.5, is based on proton resonance frequency shift (PRFS) of MRI [32], [39]–[41] which can be used to monitor the heating process and to have a closed-loop feedback control with a graphical user interface (GUI) for operator control.

According to [42], one can consider three distinct categories of HT application: superficial, deep, or whole-body hyperthermia depending on the target volume.

Superficial Hyperthermia

Superficial HT applicators are typically used to heat a limited volume of tissue close to the heating device. In general, lower frequencies heat larger and deeper regions in the body while the higher frequencies can provide localized heating of the skin and superficial tissues. Using the frequencies in the range of 400 – 1000 MHz, superficial heating within 2 – 4 cm from the skin can be obtained [42]. These heating devices can be based on waveguide/ horn antennas [44], [45] as well as low-profile, printed designs [46] and can be used to heat such superficial tumors as lymph-node metastases of H&N tumors, chest wall recurrence, breast cancer or cutaneous metastases [47]. An ex-

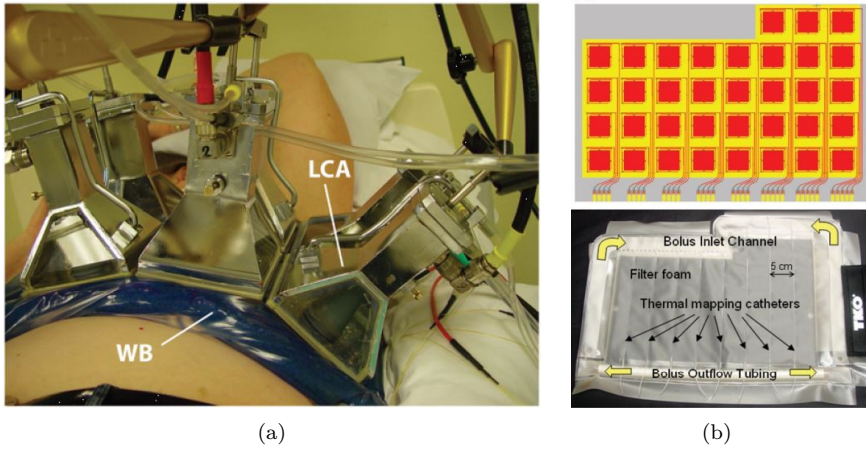


Figure 1.6: Examples of superficial applicators for local HT (a) A 2×3 Lucite Cone Applicator (LCA) array, reprinted from [45] (b) A 35-element L-shaped CMA array along with its waterbolus coupling layer, reprinted from [49].

ample of horn-based applicator, shown in Figure 1.6(a), is the Lucite Cone Applicator (LCA) working at 433 MHz to treat breast carcinomas, melanoma, and lymph-node metastasis of H&N squamous cell [44], [48]. The Conformal Microwave Array (CMA) [49], shown in Figure 1.6(b), is another example of the superficial applicators of this family that can be put around the torso of the patients and thus are low-profile and wearable. Last but not least, the 434 MHz Contact Flexible Microstrip Applicator (CFMA) and the 434 MHz ALBA ON4000 [50], [51] and the 915 MHz BSD-500 [52], [53] are clinically applied superficial systems which are routinely used in the treatment of local breast cancer recurrences [54].

Deep Hyperthermia

In deep HT, multi-antenna phased array systems are typically used to treat deep-seated tumors in large parts of the body such as the pelvic region and the limbs. Examples of such systems can be found in [29], [55]–[58]. In targets located beyond 2 cm from the skin, the temperature goal is often better

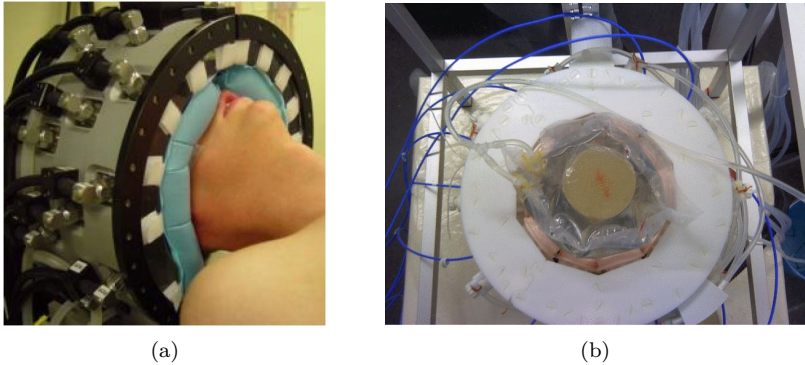


Figure 1.7: Examples of deep applicators for regional HT (a) HYPERcollar3D developed in Erasmus MC, reprinted from [61] (b) A H&N prototype developed at Chalmers, reprinted from [62].

achieved with these systems where an array of antennas is placed around the patient [42]. To create a constructive wave interference for selective heating of the target, the antennas need to be suitably fed in amplitude and phase. These steering parameters as well as the operating frequency of the antennas are determined and optimized during the Hyperthermia Treatment Planning (HTP) stage, as reviewed in [59], [60]. In a phased array system, the operating frequency is a critical parameter because it not only determines the achievable penetration depth of a certain system, but it also controls the size of the temperature focal spot which is, according to the diffraction limit, roughly around half a wavelength. Having a wide operational frequency band, Ultra-wideband (UWB) HT systems offer more degrees of freedom and flexibility.

The typical frequency for cancer treatment in pelvic region ranges from 70 to 200 MHz. Within this band, applicators from BSD 2000 family ¹ have been widely used for this purpose. BSD Sigma 60 which is the first of the two types of BSD systems is a cylindrical applicator with a ring of 8 dipole antennas and operates at 77 MHz. The second BSD applicator is Sigma Eye which is an elliptical applicator with 24 dipole antennas operating at 100 MHz.

A higher frequency range, typically above 400 MHz, has been used for hyperthermia in H&N. The group of Erasmus MC was the first to develop a

¹<https://pyrexar.com/hyperthermia/bsd-2000>

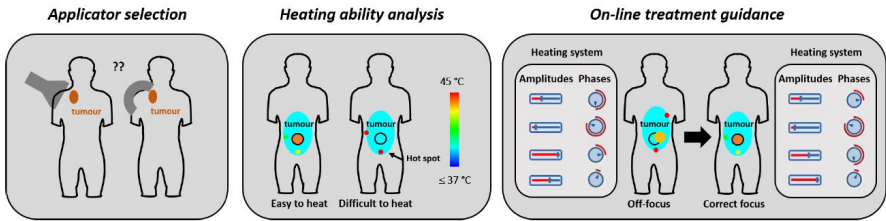


Figure 1.8: Summary of the 3 most important clinical applications of HTP (Taken and reprinted from [22]).

cylindrical applicator HYPERcollar operating at 434 MHz and consisting of 12 patch antennas for the treatment of H&N cancers [29], [63]. By proposing a 20-patch-antenna configuration over three rings, the group has recently redesigned the original applicator and branded it HYPERcollar3D [58], [64] (Figure 1.7(a)). A laboratory prototype for an Ultra-wideband H&N applicator has also been developed at Chalmers. The prototype consists of 10 self-grounded Bowtie (SGBW) Antenna [65] arranged in two interlaced rings in a cylindrical configuration (Figure 1.7(b)).

Whole-body Hyperthermia

Whole-body HT can be used to treat carcinomas with distant metastases where the cancer has expanded from the primary tumor to distant lymph nodes or organs. Soft tissue sarcomas, melanomas, or leukemia are some examples of the cancer types suitable for this type of treatment. Two systems are clinically used for this purpose by employing microwave and infrared radiation with a heating time of 60 – 90 minutes [47].

1.5 Outline of the Thesis

This thesis predominantly considers various aspects of Hyperthermia treatment planning (HTP). Applications of HTP ranges from pretreatment evaluations such as applicator selection and heating ability analysis to on-line treatment guidance [22]. Figure 1.8 summarizes these three main clinical applications, and the upcoming chapters of this thesis are arranged around each one of these applications as follows.

After introducing a new antenna model for both superficial and deep HT applications, chapter 2 investigates the process of applicator selection for the cancers occurring in the human head region. Chapter 3 focuses on beam-forming, thermal analysis, and radiobiological modelling, hence moving in the direction of heating ability analysis based on HT quality metrics. However, predictions made by pre-treatment planning are not entirely reliable due to the uncertainties in tissue properties. Therefore, hotspots and sub-optimal tumor heating can still occur. In combination with non-invasive thermometry feedback, HTP-guided steering can be helpful to improve the heat delivery during the treatment session. Chapter 4 assesses the feasibility of integrating a microwave thermometry technique into the conventional HT routines so that it can be later used as a potential candidate for a closed-loop feedback control mechanism in HT systems.

CHAPTER 2

Antenna Design

Antenna design for biomedical applications has been widely pursued by researchers in the field and has attracted attention in the past decades. These applications can be divided into two categories: therapy and diagnostics. In therapy, antennas have been used mainly for hyperthermia which has a different set of design criteria than those proposed for diagnostic purposes or free-space applications.

The antenna matching impedance in HT depends on the antenna-tissue distance determined by waterbolus dimensions, the human body region, and the patient anatomy [66]. Hence, designing an antenna that can maintain its impedance match over a practical range of distances between the antenna and the human body is a critical step towards building a good clinical HT applicator. Since human bodies with different tissues of variable dielectric properties present a high permittivity complex load to an antenna, the presence of a patient located in the antenna's radiating near-field can detune its resonance frequency, thereby impairing the EM coupling process. Conventional applicators exhibit tissue- and distant-dependent matching performance. Design strategies need to be considered to increase the resilience of the antenna against the detuning effect due to variable tissue-loading conditions. For instance, if the

applicator's operational band can be widened, the detuning effect becomes less critical as long as the detuned band still contains the desired resonant frequency feature of the nominal design [66].

In HT, focused induced heating is achieved through having a constructive interference of waves in order to make a focal point on the target. Concentrating the fields amounts to having narrow-beam radiation which requires an electrically large aperture [67]. The effective size of the aperture also plays an important role in determining the EM-field penetration profile into the body. Reflection at the interfaces between different kinds of tissues is another important factor in coupling EM energy into biological systems. The reflection at the interface of two tissues is not merely determined by the specific tissue types, but also by other factors such as the frequency, the polarization, and the angle of incident wave. When there is a large amount of reflection from these tissue interfaces, the interference between the incident and the reflected waves can result in significant standing-wave patterns that may cause excessive heating (hot spots) in certain regions of the body [67]. Ideally, it is recommended for the E-field components to be predominantly tangential to the border of these discontinuities since this will prevent overheating of superficial and interfacing tissues [66].

Aiming to contribute to the ongoing work in this active field of research, this chapter proposes a UWB, compact, shielded design which is specifically tailored to meet the requirements of modern HT devices. Furthermore, a phased array applicator based on the proposed antenna model is presented at the end of this chapter.

2.1 Design Criteria for HT Antennas

The following criteria need to be satisfied in order to have an efficient antenna design for HT applications.

- Choice of an appropriate frequency band: Biological tissues are a lossy propagation medium for EM waves, and the amount of the loss increases with frequency. On the other hand, higher frequencies give better spatial resolution and thus a smaller focal point. Therefore, when selecting the operation band of HT antennas, a compromise between these two opposing factors is needed. This has led to the selection of the lower part of the UHF band ([300 – 900] MHz) for hyperthermic purposes.

- An Ultra-wideband characteristic: UWB antennas are highly desirable for HT applications. This allows for frequency hopping to control the size of the focal point and hence to adjust it to the size of the tumors under treatment.
- A directional radiation pattern with low side-lobe levels: This provides more efficient power deposition in the patient body and also a lower level of mutual coupling and cross-talk between adjacent elements of the array.
- Size and isolation: The design should be compact and shielded from the EMC point of view.

In the literature, a variety of antenna types for high power applications of deep hyperthermia have been proposed so far [65], [68]–[70]. Applicators based on dipole [71], [72], waveguide [55], [73], and microstrip patch [29] antennas, for instance, have been in clinical use in the treatment of cervical and H&N cancer patients. While efficient, these designs are inherently narrow-band, with a fractional bandwidth no more than 5 – 10%. In an attempt to overcome the bandwidth limitation of the previous designs and to achieve a UWB design for H&N region, Takook et al. [65] tailored the self-grounded bow-tie (SGBW) design of [74] to suit the hyperthermic condition. However, to obtain a symmetric radiation field and stable electrical performance, bow-tie designs require a balun [75] which will also act as an RF-matching network. This matching network absorbs a substantial amount of power and thus decreases the efficiency of these designs [68]. Therefore, in terms of reliability and reproducibility, antennas in which an RF matching network can be avoided have a clear advantage in clinical settings [68].

The type of antenna used in an HT applicator also determines how the energy is distributed in the treated area. Many applicators are based on waveguides (WG) [55], [73] which have one of their sides closed and operate in a TE mode on the other side with an open rectangular cross-section. These hollow WGs are usually filled with distilled water and are excited by means of a short extension of loop antennas or coaxial probes [76]. The radiation resistance of the probe or loop can be made equal to the characteristic impedance of the coaxial feedline by choosing the dimensions of the coupling antenna and its position with respect to the closed end of the applicator. Compared with rectangular WGs of the same dimensions, ridged waveguides (i.e. waveguides with

a ridged cross-section) have a lower cut-off frequency, a lower characteristic impedance, and a wider frequency band free from higher-order-mode interference [77]–[79]. On the other hand, the horn-based applicators [44], which can also be considered as a variant of WG applicators by utilizing a flared opening, produce more uniform temperature fields than classical waveguides [43]. To take advantage of the positive features of both ridged waveguides and horn antennas, this thesis proposes a new design by combining the two approaches and calls it Open Ridged-Waveguide (ORWG) as follows.

2.2 The ORWG Model

Aiming for a UWB antenna suitable for both deep and superficial HT, *Paper A* proposes the design of an ORWG antenna for HT applicators. ORWG takes advantage of positive features of Double-Ridged Horn (DRH) antennas thus offering a wide band of operation. By avoiding use of a balun or RF-matching network, it avoids the problem associated with the SGBW antenna. Moreover, it is less susceptible to the cross-talks among adjacent elements as well as environmental noise and interference in general because it is inherently shielded by its metallic housing. This makes the design also appealing for diagnostic purposes like microwave imaging [80].

All the details and steps taken in the design procedure of ORWG are given in *Paper A* and therefore are not repeated here. In summary, a well-established DRH design for radar and EMC applications in the X and Ku bands [81] was scaled, filled with water, and loaded with a flat WB and muscle phantom according to the hyperthermic assurance guidelines [82], [83]. To avoid power losses in the water inside the structure and to help make the design more compact, the flaring parts were scrapped and the built-in PSO optimizer of CST¹ was used to fine-tune the parameters of the model. The PSO algorithm was set for a multi-objective optimization to yield a return loss better than -10 dB in the range of [400 – 800] MHz as well as to maximize PLD in the target tissue, i.e. muscle in this case. Figure 2.1 gives a concise summary of the design optimization workflow and the final result.

CST MW Studio 2019 provides power budget analysis whose calculation is depicted in Figure 2.2. Analysis of different power components, labeled in Figure 2.2, reveals interesting features of the optimized antenna in front of a

¹www.cst.com

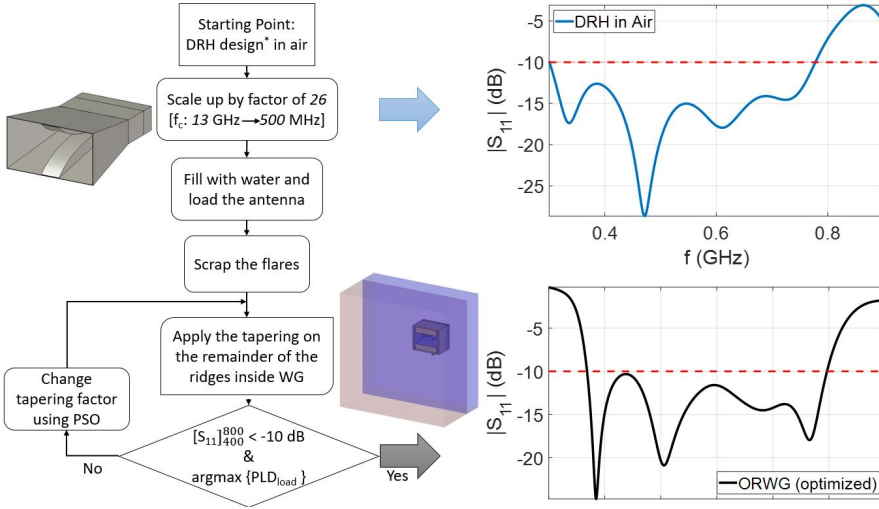


Figure 2.1: Summary of the design and optimization process of the ORWG antenna (* Original DRH from the design proposed by Mallahzadeh et al. [81])

flat WB and muscle phantom. It shows how much power is deposited in the phantom and where undesirable power losses occur. Figure 2.3(a) shows that when excited with a normalized power of 0.5 W within the desired frequency band, the antenna accepts almost all the incoming power (the blue curve) and there is a small portion of the power outgoing as the return loss (the orange curve). It is also shown that almost all the accepted power has been deposited in the dielectric materials (the red curve) with a very small amount of stray radiation outside the region of interest (the magenta curve). In this scenario, we have two dielectric materials, i.e. water and muscle. To get a better picture of how much power was successfully delivered to the target volume (muscle in this case), one can separate the volume losses in these two materials as reported in Figure 2.3(b). As can be seen, the power dissipation in water becomes larger at higher frequencies. This was expectable from the Debye model used for water in the CST simulation.

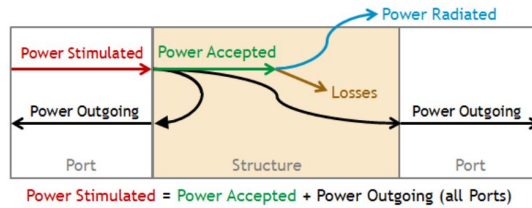
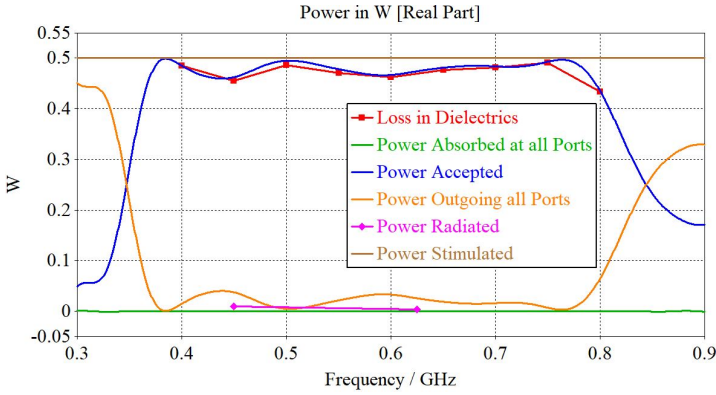


Figure 2.2: The power that is *stimulated* at one or more ports will be divided into the power which is *accepted* by the structure and the power which is again leaving the structure via the ports (*outgoing power*). Furthermore, the accepted power is converted either into *losses* (losses in dielectrics or metals) and/or is *radiated*.

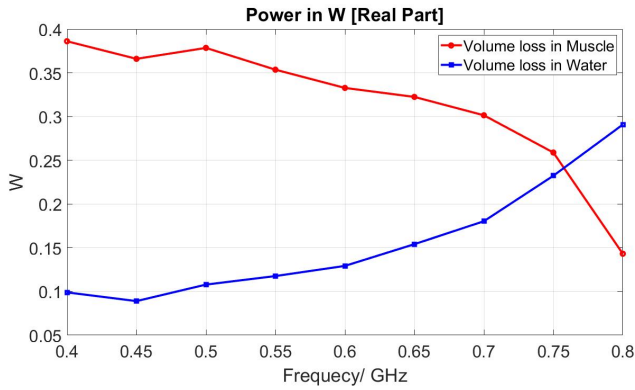
2.3 Hydrogel Bolus and Phantom Preparation

As discussed in Section 1.4, water bolus is an inseparable part of today's HT systems and plays an important role in the heating pattern of the antennas. A good WB design allows for easy positioning of the applicator around the patient, has a high level of shape predictability which is a crucial factor affecting the treatment planning performance, and is elastic enough to conform to skin contours. To form a WB, the water is typically circulated within plastic bags. Hydrogel bolus [84] has similar dielectric properties to water and is a very convenient replacement for a water-filled, plastic bag bolus. It has also been shown to provide a better enclosure between the antenna the body [84].

The hydrogel is made of 99% deionized water and 1% polymer of which 35% is LBG, another 35% is Xanthan, and the remainder 30% is Agar. The recipe and the list of ingredients for approximately 3 liters of hydrogel and muscle phantom are reported in Table 2.1. Dielectric properties of the hydrogel and phantom were measured with an open-ended coaxial dielectric probe (85070E, Dielectric Probe Kit with Performance Probe, Agilent Technologies, USA) connected to a vector network analyzer (VNA) (E8362B, Agilent Technologies, USA). Their relative permittivities are quite constant throughout the band and they read as 78 and 60 for hydrogel and muscle phantom, respectively. Their conductivities, however, slightly change within the band and they were recorded in the range of [0.3 – 0.6] and [0.4 – 1.1], respectively.



(a)



(b)

Figure 2.3: Power balance for the ORWG simulation in CST (a) All the incoming and outgoing powers along with the volume losses (b) Volume losses in each dielectric material separately.

2.4 Measurement & Verification

Far-field radiation pattern, gain, and efficiency are the design characteristics and conventional verification procedures widely used in the antenna and propagation society. Unfortunately, these metrics are not directly applicable to HT scenarios due to the propagation in lossy media [85], [86]. However, other cri-

Table 2.1: List of the ingredients used to make 3 liters of hydrogel and muscle phantom in the lab.

Ingredients	Mili-Q water (ml)	LBG (g)	Xanthan (g)	Sugar (g)	Salt (g)	Agar (g)
Hydrogel	2970	10.5	10.5	–	–	9
Muscle Phantom	2100	–	–	1665	42	66

teria defined by the HT guidelines have been proposed as viable measures for antennas' efficacy for this specific application. Since the final goal in HT is to produce a temperature gradient between the tumor and the rest of the body by raising tumor's temperature, it seems quite natural and intuitive to have a criterion to assess the capability of different antenna designs in terms of temperature rise. To this end, Equation 1.9 is usually used to relate the specific absorption rate to incremental change in temperature. According to [87], an efficient heating device for superficial HT should be able to increase the tumor temperature at a rate of 1°C per minute. Considering a typical heat capacity of muscle tissues to be around 3600, this criterion corresponds to the SAR deposition of at least 60 (W/kg). To assess if this condition was met by the ORWG design, the setup shown in Figures 2.4(a) and 2.4(b) was used in the lab. For the input power of 25 W fed to the antenna for 6 minutes, the temperature was monitored at different locations by fibre optic probes² located in the phantom according to Figure 2.4(a). Figure 2.4(c) shows the recorded temperature by the probes during the exposure and indicates that the design certainly meets this criterion.

Another criterion to appraise the efficacy of the antennas designed for HT applicators is the effective field size (EFS). The EFS is defined by the area within the 50% of maximum SAR contour in the 1 cm deep plane under the aperture. According to the guidelines, a good radiator for superficial HT needs to have an EFS greater or at least equal to its physical aperture size so that side-by-side elements in an array configuration leave no area of tissue surface uncovered. To assess the EFS experimentally, the muscle phantom was pre-cut 1 cm below its surface, and after exposure, temperature profiles were captured by an infrared camera³ at two different frequencies as reported in Figures 2.4(d) and 2.4(e). As can be seen, the performance of the antenna

²FISO Technologies, Quebec, Canada

³B355, FLIR Systems, USA

at 800 MHz is not as good as at 600 MHz and this was expected because 800 MHz is at the far end of the design's operational bandwidth where the penetration depth also starts to decline. All in all, this criterion has also been successfully met by the design (see *Paper A* for more details).

2.5 Phased Array Applicator

Annular phased arrays (APA) are the most common type of applicators used for treating deep-seated tumors in regional hyperthermia. They typically have their elements arranged in a circular or elliptical configuration around the patient's body. When it comes to selection of the right antenna design for an APA system, the impedance bandwidth is not the only deciding factor; certain minimum requirements regarding energy distribution need to be met for an applicator to be suitable for deep HT trials. The average Power Absorption (aPA) ratio has therefore been defined to quantify the relative amount of energy deposited in the tumor. If N_T and N_H are the total number of voxels in the tumorous volume (V_T) and healthy volume (V_H), respectively, then aPA is defined as

$$\begin{aligned} aPA &= \frac{\frac{1}{N_T} \times \text{Total power absorbed in the tumor}}{\frac{1}{N_H} \times \text{Total power absorbed in the healthy tissue}} \\ &= \frac{N_H \sum^{V_T} PLD}{N_T \sum^{V_H} PLD}. \end{aligned} \quad (2.1)$$

For an applicator to be deemed capable of deep heating, aPA must be greater than 1.5 [36].

Since the aim was to come up with an applicator design that would suit as many cancer cases in the human head as possible, an investigation on the optimal design for such a one-size-fits-all applicator had been performed. To this end, an anthropomorphic head phantom consisting of two regions of tumorous and average healthy brain tissues was used to evaluate the performance of three different applicators as depicted in Figure 2.5. Their performances in terms of aPA are compared in Table 2.2 which also reports the amount of the power deposited in the target and healthy tissues.

The first configuration was an elliptical annular applicator of 16 elements

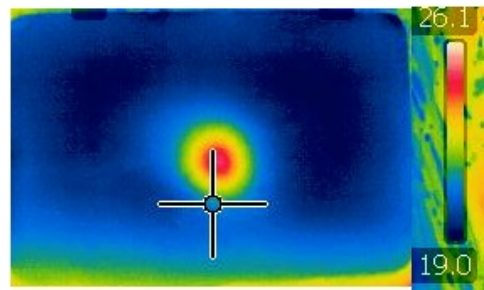
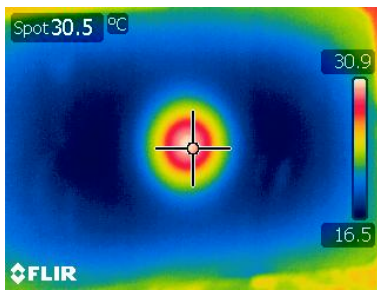
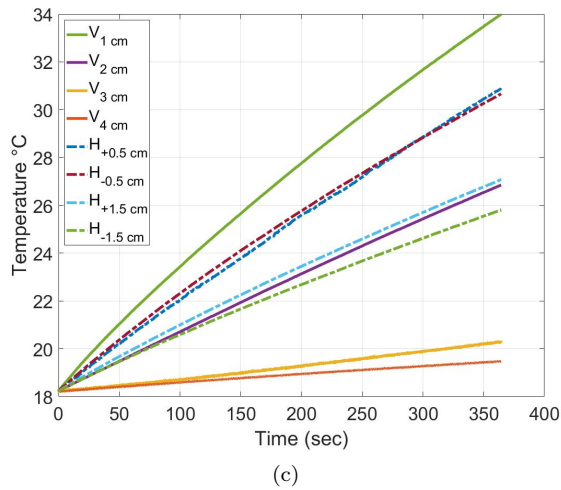
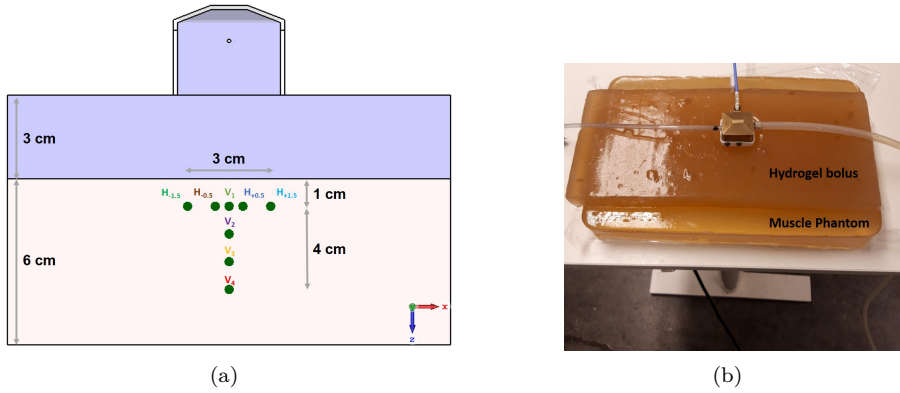


Figure 2.4: The setup used in the verification procedures (a) Schematic illustration (b) its photograph. (c) Rate of temperature change recorded by the fiber optic probes within 6 minutes of exposure at 600 MHz, and temperature profiles 1 cm below the surface of the muscle phantom captured by an IR-camera at (d) 600 MHz and (e) 800 MHz.

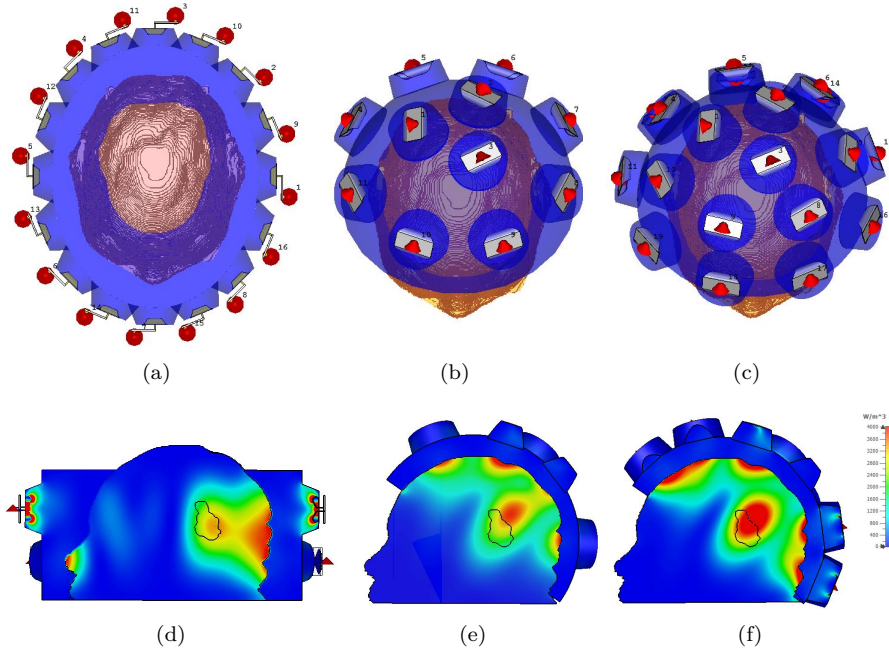


Figure 2.5: Simulation setups (1^{st} row) and PLD distributions (2^{nd} row) for the head phantom model. (a), (b), and (c) are top views of 16-element elliptical, 11-element helmet-based, and 19-element helmet-based arrangements for the antennas, respectively. (d), (e), and (f) are the corresponding PLD distributions at 450 MHz in the sagittal plane.

arranged in two rings. Some parametric studies on array parameters, similar to [88], were conducted on the dimension of the water bolus and the distance between the two rings. The optimized design had two rings with an inter-ring distance of 5 cm and a water bolus with the major axis, minor axis, and height of 14, 11, and 14 cm, respectively. The second and third configurations had a helmet-like shape with 11 and 19 elements. It should be mentioned that the old antenna model (SGBW) had been used in these simulations. However, given the comparative nature of the investigation, one should be able to generalize the result. Another subtle distinction is that the complete SGBW antenna model including its balun was used in the ring configuration

Table 2.2: Summary and comparison in terms of *aPA* among the three different array configurations used in the head phantom simulation.

Array Configurations	Annular	Helmet	
	Elliptical		
Number of Antennas	16	11	19
$\sum^{V_T \approx 13(ml)} PLD$ (W)	0.0318	0.0315	0.0445
$\sum^{V_H \approx 3600(ml)} PLD$ (W)	2.81	2.94	3.8
<i>aPA</i>	3.13	2.96	3.24

whereas the simulation of helmets did not include the balun and used discrete lumped ports right at the location of the antenna pins.

As can be seen from Figure 2.5(e), the configuration with 11 elements for the helmet design does not guarantee deep enough penetration to reach the target. The configuration with 19 elements, on the other hand, is rather effective but at the expense of more stray losses deposited in the healthy tissue. It is also more complex hardware-wise and requires more input power due to the higher number of antennas. Performance of the ring configuration is somewhere in the middle, showing results between those two bounds achieved by the helmet designs. It provides good coverage of the tumor with the lowest level of stray losses deposited outside the target.

Based on the *aPA* metrics, level of the undesired power deposition in healthy tissue, and the number of antennas, the elliptical ring configuration was selected as the optimal design for *Paper B*. This selection is in line with the conclusion made by other groups active in the field. Oberacker et al. [39], for instance, showed that the best results in a power optimization sweep are obtained for a 16-element interleaved RF applicator using an elliptical antenna arrangement with water bolus.

To test the power deposition capability of the ring configuration with ORWG antennas, two realistic and very challenging cancer cases of the pediatric medulloblastoma and adulthood central nervous system (CNS), shown in Figures 2.6(a) and 2.6(b), were further considered at the frequency of 400 MHz. Dielectric properties reported in Table 2.3 were used for the child model and those related to the CNS-Duke model were taken from the IT'IS database [89]. The built-in PSO optimizer of CST was used to maximize their *aPA* ratios. The optimum values of 4.5 and 4.8 were obtained for the medulloblastoma

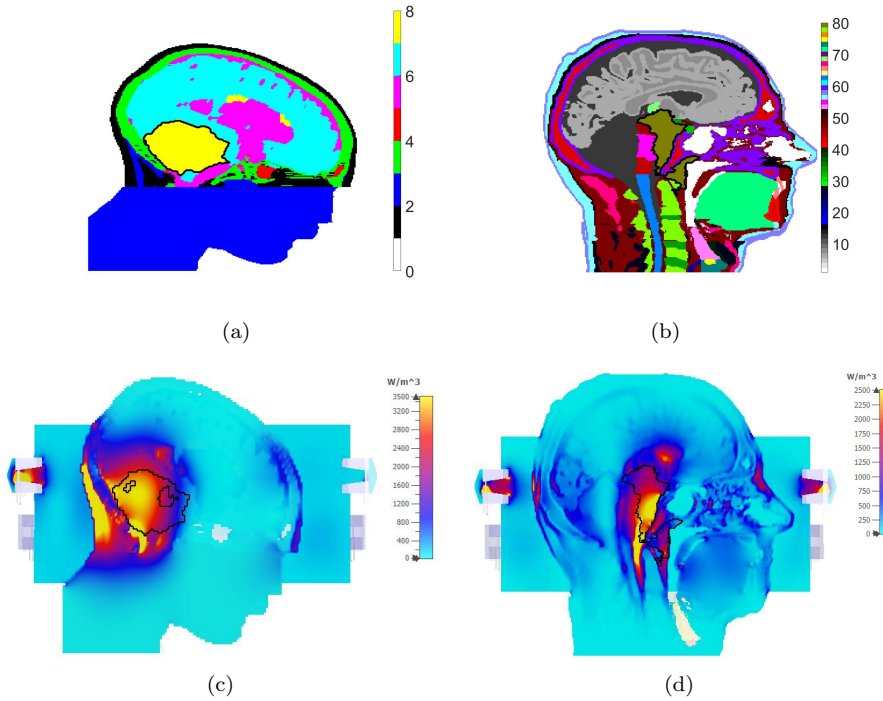


Figure 2.6: Sagittal cross-sections of the realistic models for (a) a child with a big medulloblastoma tumor and (b) an adult with a tumor in CNS. (c) and (d) are their corresponding PLD distributions (solid black lines show the border of the tumors).

and CNS scenarios, respectively.

Compared to the Duke model where there are more than 45 tissue types, the child model has only 10 tissue types which makes it very convenient to tabulate the amount of power absorbed by each tissue type as in the last column of Table 2.3. Out of 3.95 W of the stimulated power, 3.72 W has been absorbed by the dielectrics of which 0.85 W is the share of water. The normalized absorbed power per volume of each tissue type is reported in Figure 2.7.

Table 2.3: Dielectric properties of the tissues and the power deposited in them in the simulation of the child model at 400 MHz (σ : electric conductivity, ϵ_r : relative permittivity, ρ : density).

Tissue Type	Index	σ [S/m]	ϵ_r	ρ [kg/m ³]	Volume (ml)	$\sum^V PLD$ (W)
Skin	1	0.73	44.9	1109	496	0.76
Muscle	2	0.82	56.4	1090	1633	0.51
Bone	3	0.1	12.9	1908	438	0.18
CSF	5	2.28	70.1	1007	341	0.32
Gray matter	6	0.78	55.8	1045	1007	0.68
White matter	7	0.47	41	1041	124	0.04
Tumor + Cyst	8	0.85	56.6	1056	126	0.35
Eye	9	1.54	68.9	1005	18	0.02
Cartilage	10	0.62	44.6	1099	6	0.014

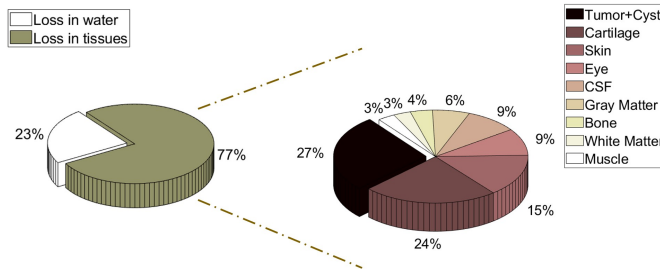


Figure 2.7: Normalized power dissipated per occupied volume of each tissue type of the child model separately.

Hyperthermia Treatment Planning

Hyperthermia treatment planning (HTP) is a process in which a set of treatment parameters are established by EM and thermal modellings to maximize the treatment quality [59]. HTP simulation tools can be used to develop enhanced treatment approaches or, retrospectively, to analyze treatment quality. In recent years with the introduction of more powerful EM simulation tools and software packages capable of handling thermal simulations, HTP has begun to appear in the clinical HT routines because of its ability to predict clinical outcomes [22]. It helps evaluate the effectiveness of different scenarios before HT sessions to aid in the selection of applicator or treatment approach and specific power excitation planning. In addition, simulations are helpful for assessing treatment risks to the patient or operator.

As depicted in Figure 3.1, simulations for HTP can be divided into three distinct tasks summarized below and further elaborated upon each separately in the subsequent sections.

1. **Generation of the patient model for Computational Electromagnetics (CEM):** Starting with patient data acquisition, the geometry and tissue properties of the involved body region must be carefully determined. Using Computed Tomography (CT) or Magnetic Resonance

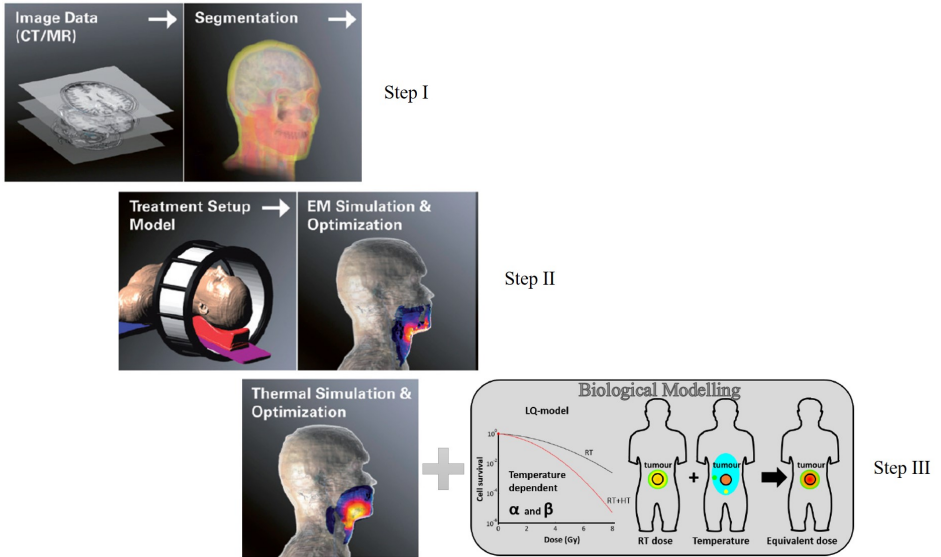


Figure 3.1: Schematic workflow for EM-HTP (Reprinted from [59] and [22]).

Images (MRI) of the actual subject, manual or semi-automatic segmentation needs to be performed to obtain the patient-specific model.

2. **Calculation of the PLD/ SAR distributions in the tissue:** Patient's model and a model of the applicator with the required degree of complexity are combined and used to compute the PLD/ SAR distribution.
3. **Calculation of the resulting temperature distribution and post processing analysis in case of a combined treatment modality:** Once the PLD pattern is established, the temperature (T) distribution can be predicted considering the impact of physiological aspects such as perfusion and core temperature. In synergistic treatment modalities like thermoradiotherapy, a further step can be also taken to quantify the radio-sensitizing effect of hyperthermia.

3.1 Step I. Human Models for CEM Research

Realistic computational human models or 'virtual humans' are becoming a significant component of modern biomedical research. The Virtual Population from IT'IS Foundation Switzerland [90], [91] is certainly one of the most comprehensive model families for CEM and radiological simulations. Major members of the virtual population are shown in Figure 3.2 and tabulated in Figure 3.3.

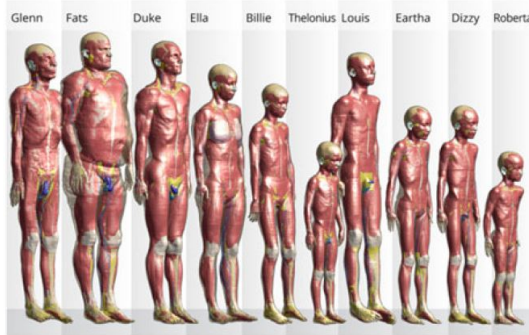


Figure 3.2: Member of IT'IS Virtual Population – Voxel models.

A vast majority of the virtual-human models available are voxel models and not CAD models. The difference between CAD and voxel models is quite significant and influences both the type of the CEM problems to be solved (resonant or not) and the EM solver type [92]. Voxel-based models naturally represent highly-inhomogeneous inter-tissue regions and can replicate these tissues exactly as they appear in the source images. This is not the case with 3D CAD models of a multi-tissue body as they are much more difficult to construct. Furthermore, detailed triangulated human models with a very large number of triangles can be very computationally expensive, both in terms of FEM meshing times to create a volumetric tetrahedral mesh and in terms of FEM simulation times. This can make their use prohibitive for a number of optimization tasks.

On the other hand, triangular- or quadrilateral-based CAD models have a clear mathematical advantage which is a linear surface approximation in contrast to the staircase approximation of the voxel grid. In fact, the segmentation accuracy which is the deviation from the true surface along the normal

Model Name	G/A/H/W	Da	TYPE	RES, mm ³	FV	D
Glenn	m/84/173/61.1	N	V	0.5x0.5x1.0h 0.9x0.9x2b	N	Y
FATS	m/37/182/119	N	V	0.5x0.5x1.0h 0.9x0.9x2b	N	Y
DUKE	m/34/177/70.3	N	V/S	0.5x0.5x1.0h 0.9x0.9x2b	Y	Y
ELLA	f/26/163/57.3	N	V/S	0.5x0.5x1.0h 0.9x0.9x2b	Y	Y
LOUIS	m/14/168/49.7	N	V	0.5x0.5x1.0h 0.9x0.9x2b	N	Y
BILLIE	f/11/149/34.0	N	V/S	0.5x0.5x1.0h 0.9x0.9x2b	Y	Y
EARTHA	f/8/136/29.9	N	V	0.5x0.5x1.0h 0.9x0.9x2b	N	Y
DIZZY	m/8/137/25.4	N	V	0.5x0.5x1.0h 0.9x0.9x2b	N	Y
THELONIOUS	m/6/115/18.6	N	V/S	0.5x0.5x1.0h 0.9x0.9x2b	Y	Y
ROBERTA	f/5/109/17.8	N	V	0.5x0.5x1.0h 0.9x0.9x2b	N	Y
NINA	f/3/92/13.9	N	V	0.5x0.5x1.0h 0.9x0.9x2b	N	N
CHARLIE	f/8w/na/4.3	N	V	0.5x0.5x1.0h 0.9x0.9x2b	N	N

Figure 3.3: G/A/H/W—Gender/Age/Height/Weight; Da—Original image dataset made available for independent evaluation (Y/N); TYPE (V—voxel; S—surface-based model, but without proven FEM meshability); RES—Lowest image resolution (before or after post-processing) of the model declared by the provider (h = head, b = body); FV—Free version availability (Y/N); D—Deformable/posable (Y/N). Rerinted from [92].

direction is equal to the size of the unit cell for voxel models. Moreover, voxel models are inflexible to deformations while the CAD models are inherently deformable including both free-form deformations and affine transformations [92]. Last but not least, CAD models are fully compatible with the standard FEM analysis on unstructured grids and 3D printing while the voxel models are not.

The two realistic models used in this chapter are shown in Figure 3.4. The first model, henceforth called case-study 1 in this chapter, is the head of the Duke model from IT’IS which was down-sampled to the resolution of 2 mm for the sake of faster simulations and a tumor was inserted in the tongue region as shown in red in Figure 3.4(a). The second model, henceforth called case-study 2 in this chapter, is the same as the one presented in chapter 2. The

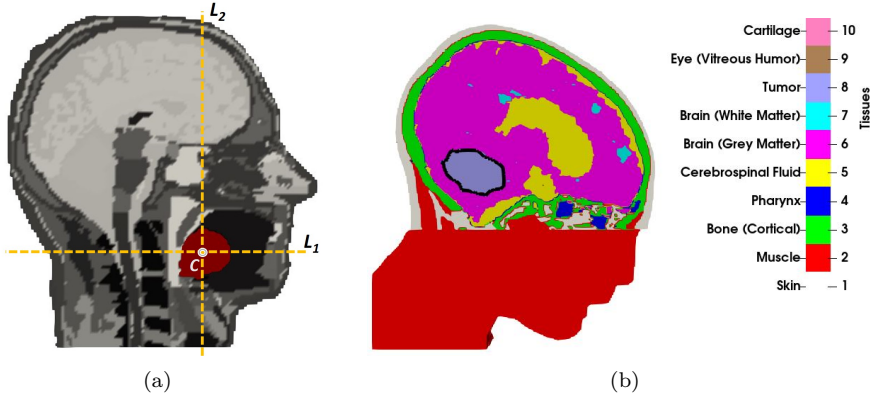


Figure 3.4: Sagittal cross-sections of (a) The Duke model with a tumor shown in red in the tongue region – L_1 and L_2 are 2D cut-lines for thermal validation and C is the center of the tumor where the two lines intersect (b) The child model with shrunken medulloblastoma.

only distinction is that the original tumor was too large for radiosurgery with γ -knife and was thus reduced to 34 mL by means of morphological operations. This model was manually segmented from an MRI scan with a $1 \times 1 \times 1$ mm resolution of a 13-year old boy with medulloblastoma treated at Sahlgrenska University Hospital. Note that only a part of the head was segmented, and the section outside the treatment volume was modelled as muscle.

3.2 Step II. EM Simulation & Optimization

EM Field Simulation

The type of EM technique used depends on the human model availability. e.g. voxel or CAD. Voxel-based models on uniform rectangular grids lend themselves primarily to finite-difference (FD) methods [93] at low frequencies and to the FD time-domain (FDTD) methods at high frequencies [93]–[95]. For high frequency EM simulations which involve computational human models, FDTD is currently the major tool. The time domain EM solver of CST uses a variant of this method called finite integration technique (FIT) [96], [97]

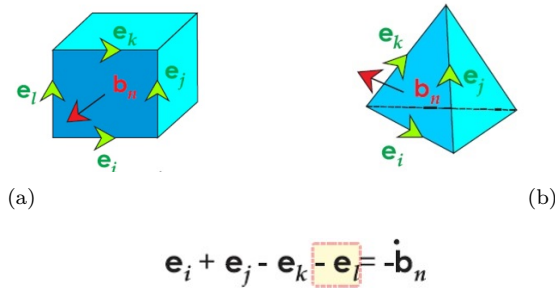


Figure 3.5: Using FIT to discretize Faraday’s equation for (a) a cube – similar to the FDTD Yee cell (b) a tetrahedral mesh.

which is reduced to the standard FDTD on a uniform rectangular grid as shown in Figure 3.5(a) and can simultaneously expand the FDTD method to tetrahedral grids as shown in Figure 3.5(b).

A CAD-based human model is suitable for the Finite Element Method (FEM). Both commercial software packages of ANSYS HFSS¹ and Comsol² use FEM as their computational engine for EM simulations. For radio wave propagation, the FEM method has been primarily implemented in the frequency domain which can better resolve resonances. For MRI-related research, for instance, the frequency domain FEM method may significantly outperform FDTD computations [98]. This partly stems from the fact that FEM has a powerful adaptive mesh refinement scheme that enables tetrahedral mesh optimization in such a way that despite a significant reduction in the computational runtime, the simulation can still be handled accurately. For complicated geometries, the use of unstructured meshes combined with automatic mesh adaptation in the frequency domain is instrumental in delivering accurate results [92]. On the other hand, it has been traditionally difficult to implement FEM methods in the time domain for a broadband system response. To tackle this issue, discontinuous Galerkin schemes have been developed [99].

¹www.ansys.com/ansys-hfss

²www.comsol.com/comsol-multiphysics

SAR-based Optimization

For HTP routines, a focusing technique that guarantees the formation of a focal point at the tumor's location is of paramount importance. In other words, a good power deposition scheme avoids creating hot spots which are excessive focal points formed outside the targeted region. Associated with all the focusing techniques proposed in this context are such heated topics as hot spot suppression and multi-target beamforming based on either specific absorption rate (SAR) or temperature. In fact, whether SAR, as is the case in this thesis, or temperature should be optimized is still a matter of debate [100]. Although the final goal of the treatment is to generate a temperature gradient between tumor and healthy tissue, all the potential benefits of direct temperature optimization may be lost under the heavy computational burden due to large uncertainties in thermal modeling [101]. Moreover, Lee et al. [102] demonstrated a good correlation between SAR coverage indicators and clinical outcomes of HT.

Because the problem of finding appropriate excitations for each individual channel in an RF/MW applicator is non-convex, finding the global optimum has proven to be challenging and computationally expensive. To tackle the issue, several beamforming methods have been proposed in the literature among which we count the generalized eigenvalue problem (EGV) [103], time reversal (TR) [104], particle swarm optimization (PSO) [105], focusing via constrained optimization (FOCO) [106], [107], and multiplexed vector field shaping (MVFS) [108].

While fast and efficient, the EGV is highly dependent on its functional definition. For instance, other indicators like hotspot-tumor quotient (HTQ), which has so far shown the most successful correlation with clinical results [109], cannot be used as the functional for this method. Moreover, the method does not allow for simultaneous optimization of multiple frequencies. TR is a fast and popular method widely used in the literature, albeit with several limitations: (a) due to the emergence of ghost focal points, TR's focusing capability decreases for the large target areas (b) the performance is highly dependent on the selection of 'virtual source position'. PSO and FOCO are more computationally demanding, but they offer more flexibility when it comes to beam-shaping and the adoption of different fitness functions. Using only the predominant field component at a single or a very few points in a scalar regime, FOCO linearizes the problem which may not lead to the optimal solution if

the assumption of a single dominant component in the target region does not hold true. Like FOCO, MVFS falls into the category of convex optimization approaches but with the distinction that there is no linearization in its formulation and hence it is not scalar. MVFS casts the constrained RF/MW heating problem into a semi-definite program of a time- and frequency-multiplexed iterative optimization algorithm and quickly solves it to global optimality.

To find the optimum excitations for antenna elements of the proposed applicator, this chapter utilizes PSO while taking advantage of TR fast computation by using it as the starting point. It goes without saying that using an educated initial guess can help to reduce both the optimization time and the odds of getting trapped in local minima.

Implementation of PSO in EM problems is straightforward as discussed elsewhere [110]. The main steps taken are listed below.

- **Definition of the problem space:** if N is the number of antennas, then the goal is to find N complex numbers (each has a phase and amplitude that is normalized to the maximum in the set) in such a way that they make a focal point on tumor when excited simultaneously. To this end, 15 particles are set to search the solution space of a unit circle in the complex plane. So each particle is an N by one vector of complex numbers in that space.
- **Initialization of the 1st swarm:** TR setting is assigned to the first particle in the set because we want to take advantage of having a good initial guess and to expedite the whole process of the optimization. The rest of the particles are initialized by being assigned random complex numbers in the search space.
- **Cost Function:** a well-defined goal function is the key to every successful optimization problem. Although there are a lot of different indicators defined in the literature to reflect SAR distribution in tumor's volume, HTQ so far seems to be the most promising, showing a better correlation to clinical outcomes. Therefore, it is selected as the cost function here as follows

$$HTQ = \frac{\overline{SAR}(V_{1\%})}{\overline{SAR}(T)} \quad (3.1)$$

where $\overline{SAR}(V_{1\%})$ and $\overline{SAR}(T)$ are the highest percentile of SAR distribution in the healthy tissue and the mean SAR absorbed by the tumor, respectively.

- **Termination condition:** the optimization is terminated when the maximum number of iterations (M) or the maximum number of stall iterations (S) is reached, whichever comes first. In this problem, M and S are set to 30 and 5, respectively.

Given that the size of tumors is different in these two scenarios, with case-study 2 having a much larger tumor volume, 500 MHz and 400 MHz are selected for case-study 1 and 2, respectively. Results of the cost function minimization and beamforming for case-study 1 have been reported in *Paper B* and thus not repeated here. The corresponding results for case-study 2 are shown in Figure 3.6. As can be seen from the plot, the hyperthermia treatment plan resulted in an HTQ value of 1.53 in less than 30 iterations. SAR treatment quantifiers of target coverage 25% (TC_{25}) and 50% (TC_{50}) were measured to be $TC_{25} = 97\%$ and $TC_{50} = 78\%$. TC_x indicates the percentage of the tumor volume that is enclosed by the iso-contour of $x\%$ of the maximum deposited SAR in the tumor.

3.3 Step III. Thermal Simulation

To fully understand and evaluate HT treatment session, SAR simulations need to be followed by thermal analysis in order to account for relevant cooling mechanisms as tissue perfusion and water bolus cooling. The most widely used model for this purpose is the Pennes Bioheat equation [111]. While computationally efficient, Pennes equation provides a simplified model for the phenomenon as it fails to account for the direction of the blood flow or heat exchange between large blood vessels and tissue. Van den Berg et al. [112] have shown that this can result in significant inaccuracies in temperature prediction of about $1 - 2^\circ C$. To address the issue and to improve temperature predictions in HTP, advanced thermal models such as DIVA which includes large discrete vasculature have been developed [113]. These advanced models are, however, computationally expensive and require GPU-based algorithms for a fast and efficient implementation. Moreover, a detailed and adequate estimation of blood flow during hyperthermia which is an important input

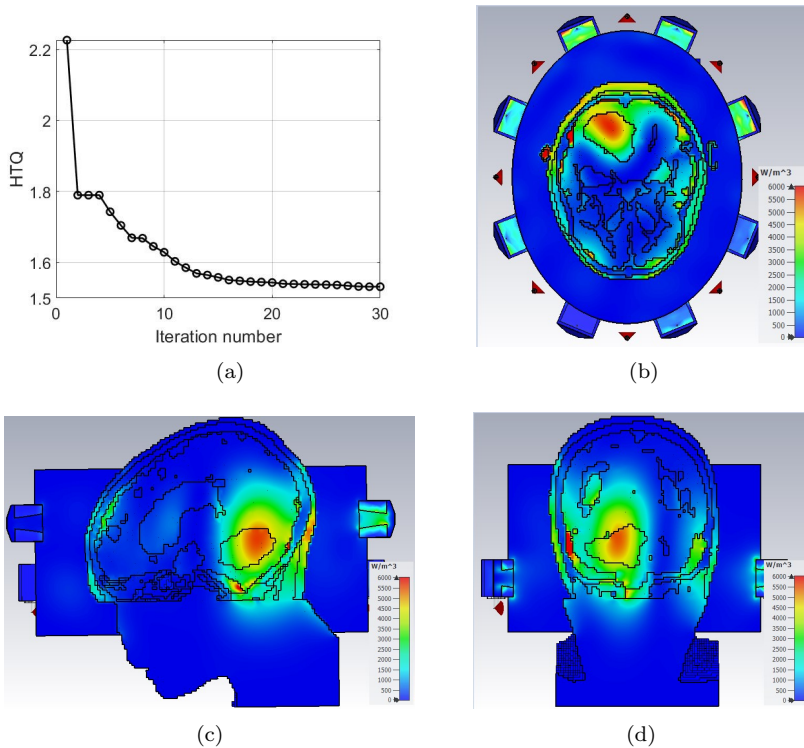


Figure 3.6: (a) TR-PSO for minimization of the HTQ at 400 MHz (b), (c), and (d) PLD distributions for the normalized excitation power of 0.5 W per channel in transverse, sagittal, and coronal planes, respectively.

parameter to these models remains challenging and subject of further research [22].

While commercial solvers like CST and Comsol can be used to tackle such a multi-physics problem to some extent, a modular open-source computational engine provides more flexibility to model, simulate, and optimize the treatment planning workflow. It can also save computational time upon efficient implementation. Moreover, CST uses only hexahedron meshes for thermal simulation of biological models which limits the ability of its solver to conform the meshes to the natural curvatures of the biological structures/ tissues. As a

result, it can give rise to staircase approximations at tissues borders. Comsol, on the other hand, uses the tetrahedron mesh type, which is more flexible for conformal meshing, but at its current implementation, Comsol's mesh generator package cannot handle very sophisticated structures like human bodies with lots of intricate tissue geometry. Despite the availability of a possible workaround suggesting the dielectric mapping instead of importing the whole physical body model into Comsol [114], [115], this solution introduces additional approximation due to dielectric interpolation at tissue borders.

Development of a FEniCS-based Thermal Solver

In this section, Pennes Bioheat equation (1.10) in conjunction with the Dirichlet boundary condition of $T = T_{bolus}$, i.e. a fixed water bolus temperature at the border of the computational domain, has been considered for thermal modelling. A brief overview of the theoretical approach to model the physical phenomenon is first given and the integral 'weak forms' are derived. Then the open-source codes of the Finite Elements of nonlinear iterative Computational Science (FEniCS) project [116] have been used to numerically solve the integral forms. FEniCS uses the Unified Form Language (UFL) which provides a flexible interface for defining expressions for weak forms in a notation close to mathematical notations and can be scripted either in C++ or Python. The Python distribution of Anaconda³ with its powerful IDE, Spyder, which resembles and includes most of Matlab's functionalities has been used for the thermal analysis in this study. Finally, the results of FEniCS are presented and crosschecked against Comsol.

In the context of finite element method, boundary-value problems can be solved either using the variational method of Rayleigh-Ritz or the weighted residual method of Galerkin to formulate the elemental FEM equations [117]. In the Rayleigh-Ritz method, the boundary-value problem is formulated in terms of a variational expression, called functional. The minimum of this functional corresponds to the governing differential equation under the given boundary conditions (BC). Natural BCs are automatically satisfied in the process of minimization or maximization of the functional. Essential BCs, on the other hand, have to be explicitly enforced, hence the name 'essential'. Galerkin's method, which belongs to the family of weighted residual methods, seeks the solution by weighting the residual of the governing differential

³www.anaconda.com

equation. The weighting functions in this method are selected to be the same as the basis functions used for the expansion of the approximate solution (see [117], [118] for a thorough discussion on the subject).

The weak form of Equation 1.10 can be derived by considering $\frac{\partial T}{\partial t}$ as $(T^{n+1} - T^n)/\Delta t$ which is a central finite difference discretization of the n^{th} time step

$$\begin{aligned} \frac{c\rho}{\Delta t}(T^{n+1} - T^n) &= \kappa \nabla^2 T^{n+1} + PLD - c_b \omega_b (T^{n+1} - T_b) \\ T^{n+1} - T^n - \frac{\kappa \Delta t}{c\rho} \nabla^2 T^{n+1} - \frac{\Delta t}{c\rho} PLD + \frac{c_b \omega_b \Delta t}{c\rho} (T^{n+1} - T_b) &= 0. \end{aligned} \quad (3.2)$$

By multiplying Equation 3.2 with the weight function w and integrating it over the computational domain Ω , we get

$$\int_{\Omega} \left[T^{n+1} w - T^n w - \frac{\kappa \Delta t}{c\rho} \nabla^2 T^{n+1} w - \frac{\Delta t}{c\rho} PLD \cdot w + \frac{c_b \omega_b \Delta t}{c\rho} (T^{n+1} - T_b) w \right] d\Omega = 0.$$

The 'weak form' means reducing the second-order derivative of $\nabla^2 T$ to a first-order derivative using By-part integration for higher orders. The product rule for divergence from vector identities in mathematics states that $\nabla \cdot (w\mathbf{V}) = w\nabla \cdot \mathbf{V} + \nabla w \cdot \mathbf{V}$ for a given vector \mathbf{V} and a scalar w . Now, considering $\nabla^2 T^{n+1}$ as \mathbf{V} , the following mathematics manipulation can be performed

$$w \nabla^2 T^{n+1} = w \nabla \cdot \nabla T^{n+1} = \nabla \cdot (w \nabla T^{n+1}) - \nabla w \cdot \nabla T^{n+1}$$

which can be further simplified using the divergence theorem to get

$$\int_{\Omega} w \nabla^2 T^{n+1} d\Omega = \int_{\partial\Omega} w \nabla T^{n+1} d\Gamma - \int_{\Omega} \nabla w \cdot \nabla T^{n+1} d\Omega. \quad (3.3)$$

According to the essential Dirichlet BC and the fact that we have no variation on the border, the first term in the right-hand side of Equation 3.3 vanishes and the substitution of the second term into Equation 3.2 gives the following weak form equation

$$\int_{\Omega} \left[T^{n+1} w - T^n w + \frac{\kappa \Delta t}{c\rho} \nabla w \cdot \nabla T^{n+1} - \frac{\Delta t}{c\rho} PLD \cdot w + \frac{c_b \omega_b \Delta t}{c\rho} (T^{n+1} - T_b) w \right] d\Omega = 0. \quad (3.4)$$

Finally, using the UFL notation, Equation 3.4 can be written in a Python script as the symbolic Bioheat equation ($F_{n+1}(T; w) = 0$) and then FEniCS can be asked to separate the linear ($L(w)$) and bi-linear ($a(T, w)$) parts and solve the equation. Interested readers can consult [119] for detailed instructions on how to write a UFL Python script for heat equations in general. Note that the steady-state analysis can also be easily performed by setting $\frac{\partial T}{\partial t}$ in Equation 1.10 to zero and repeating the weak form calculation as discussed above.

Following the instructions in its official website⁴, the latest stable version of FEniCS can be installed on a Linux distribution such as Ubuntu⁵ or on the Windows Subsystem for Linux (WSL)⁶ in a Windows-based machine. After a successful installation of the platform and having the weak form Equation 3.4 scripted in Python and ready, the next step is to import the geometry and the mesh into the platform. FEniCS itself does not provide the necessary tools and functionalities to mesh very complex scenarios such as human bodies with very heterogeneous properties, but it accepts most common mesh types produced by other dedicated mesh generators. In particular, it provides two mesh converters, i.e. *dolfin-convert* and its modern version *meshio*, to convert the imported meshes to the *xml* format for its internal processes. A powerful Matlab-based meshing toolbox called Iso2mesh⁷ is used in this study to mesh the scenarios. Iso2mesh allows for the tissue-specific assignment of blood perfusion rate and other thermal properties by giving each tissue type a unique identifier. It can also save the meshes in the *Gmesh*⁸ format that can be later imported, converted, and used by FEniCS. To compute the solution, FEniCS offers a variety of linear solver methods based on either Krylov iterative solvers such as Conjugate gradient (Cg) and Generalized minimal residual (gmres) methods with different pre-conditioners or direct LU-decomposition methods such as PETSc and Multifrontal Massively Parallel Sparse direct Solver (MUMPS). The appropriate selection of the solver depends on the scenario, the number of mesh cells, available RAM of the operating computer, desired accuracy, and the run-time. After running the simulation, FEniCS can output the result in *HDF5* or *vtk* formats. The latter is a very convenient

⁴www.fenicsproject.org

⁵www.ubuntu.com

⁶<https://docs.microsoft.com/en-us/windows/wsl/about>

⁷www.iso2mesh.sourceforge.net

⁸www.gmsh.info

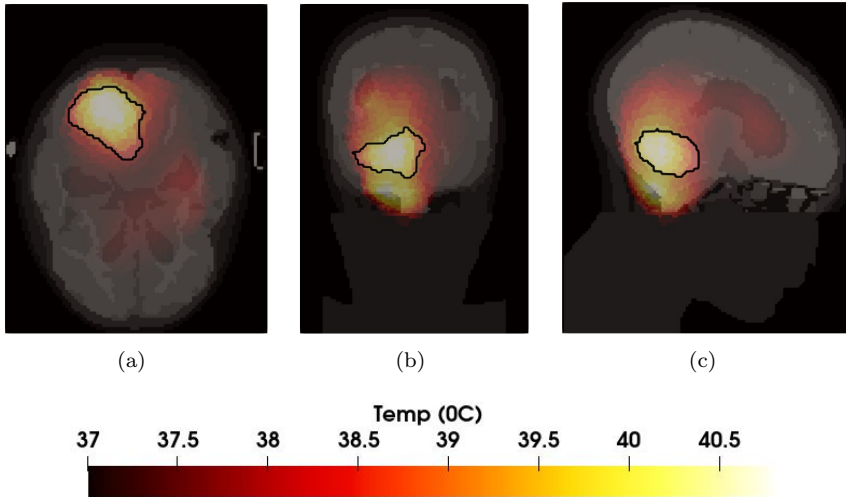


Figure 3.7: Temperature distributions for case-study 2 in (a) transverse, (b) coronal, and (c) sagittal planes.

choice for post-processing and visualization in ParaView⁹.

Thermal Evaluation & Analysis

After exporting the EM fields from CST, thermal analysis for both case-studies were performed using FEniCS. Steady-state temperature distributions for case-study 1 has been reported in *Paper B* and those of case-study 2 are shown in Figure 3.7. To quantify the quality of the treatment outcome based on commonly used metrics in the HT community, thermal indicators of T_{90} , T_{50} , T_{10} were measured as follows: $T_{90} = 38.57^{\circ}C$, $T_{50} = 39.79^{\circ}C$, and $T_{10} = 40.77^{\circ}C$. The thermal indicator of T_x determines the temperature in the target tumor exceeding by x percent of all the temperature values.

The thermal distribution obtained for case-study 1 was compared to that of Comsol. As stated earlier, we do not expect to see identical results due to limitations associated with the current implementation of Comsol. Figures 3.8(a) and 3.8(b) present the steady-state temperature distributions computed

⁹www.paraview.org

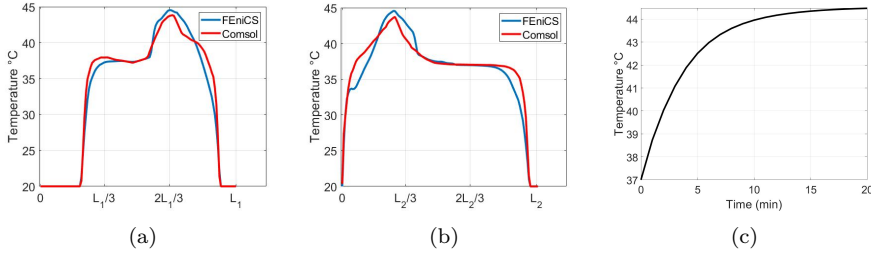


Figure 3.8: Steady-state temperature profiles of case-study 1 simulated both by FEniCS and Comsol along (a) L_1 (b) L_2 . (c) Transient temperature evolution in the center of the tumor (point C) over a time window of 20 minutes simulated by FEniCS.

by FEniCS and Comsol along the cut-lines L_1 and L_2 that run through the center of the tumor and are shown in Figure 3.4(a). As can be seen, there is a good agreement between the two solvers in general. The predicted distribution of FEniCS is, however, smoother than Comsol because of the finer meshes employed. The highest possible number of mesh cells that Comsol could handle for this scenario was used. Yet, as the sharp edges in red curves indicate, the number of mesh cells in Comsol needs to be higher to obtain a smoother thermal distribution. For the transient analysis, Figure 3.8(c) shows how temperature at the center of the tumor (point C in Figure 3.4(a)) evolves during a time window of 20 minutes of HT application. After almost 15 minutes, the steady-state condition reaches with temperature plateauing at 44.5°C . The transient result is presented only for the FEniCS case because the Comsol solution did not converge at the end due to the spatial resolution of the meshes and its impact on the temporal steps. On the contrary, a Crank-Nicolson scheme for temporal steps in FEniCS was utilized which guaranteed the convergence in a reasonable deal of simulation time. Below, the temporal stability is briefly elaborated upon.

As mentioned earlier, the central FD scheme for temporal steps was used to obtain Equation 3.4. There are, however, other schemes more capable of handling transient problems for complex geometries where there are very fine and detailed mesh cells. This intricacy of the mesh can have an implication on the numerical stability and convergence of the method. The so-called θ -

scheme offers three discretization methods in one notation as follows

$$\frac{c\rho}{\Delta t}(T^{n+1} - T^n) = \kappa\theta\nabla^2 T^{n+1} + \kappa(1-\theta)\nabla^2 T^n + \theta f(t_{n+1}) + (1-\theta)f(t_n) \quad (3.5)$$

where f is the source/ sink term. Depending on the value of θ , Equation 3.5 can be considered as the explicit Euler scheme, for $\theta = 0$; the Crank-Nicolson scheme, for $\theta = \frac{1}{2}$; or the implicit Euler scheme, for $\theta = 1$.

3.4 Radiobiological Modelling

Radiotherapy (RT) is a curative treatment modality, but the radiation dose needed to eradicate cancerous cells may inflict acute or long-term side effects such as radiation-induced tissue fibrosis and second malignancies [120]. Hyperthermia is known to be a potent radiosensitizer [121], [122]. This means the same local tumor control can be achieved using less radiation dose in the combined RT-HT treatments, thereby lowering the chance of adverse effects of radiation in the adjacent normal tissues [123], [124]. The scheduled sequence of the RT and HT and the time interval between them determine the efficacy of the combined RT-HT treatment where the best outcome for the patient is expected from a simultaneous application [125]–[127].

In this context, mathematical methods for the prediction of the therapeutic outcome of various combined treatment schemes are (a) essential to better understand the synergistic therapeutic window and (b) highly relevant to the design of adequate and individualized treatment planning in the clinical setting [128], [129]. Several mathematical models for RT- and HT-alone treatments have been proposed in the literature, but there is poor consensus about the efficacy of the combined treatment regime and the way to model it [130]. For RT, the LQ-model, described in more detail later, is the most extensively used approach to predict the effect of irradiation on cell populations [131], [132]. Regarding HT, there is considerable literature describing the impact of heat on different cellular components [133], [134], and several models are aimed to predict the survival of cells under HT treatments among which is the Arrhenius model [135], [136].

Radiosurgery with Leksell Gamma Knife

In 1951, Swedish researchers developed the concept of radiosurgery to stereotactically direct a single high dose of radiation to the intracranial region [137]. The word stereotactic refers to the functionality of the treatment planner to identify the 3D coordinate systems of the diagnostic images and the actual position of the patient and is commonly used as a prefix to radiosurgery, i.e. stereotactic radiosurgery (SRS). Ionization of the target tissue by means of high-energy radiation, usually Gamma radiation, is the fundamental principle of radiosurgery. Through ionization, the number of ions and free radicals which are harmful to the cells will increase, resulting eventually in cell death by producing irreparable damage to DNA, proteins, and lipids.

The precise irradiation of targets within the brain is planned in SRS using information from diagnostic images obtained by Computed Tomography (CT), Magnetic Resonance Imaging (MRI), Positron Emission Tomography (PET), or angiography. The radiation dose is usually measured in Gray (Gy) which is the absorption of one Joule per kilogram of mass. Compared to traditional radiotherapy treatments which are typically delivered in 30 fractions over a period of 10 weeks, an advantage of SRS is the delivery of a high amount of radiation to the tumor in one or a few fractions. Moreover, due to the sharp dose gradients in SRS, treatments are given with extremely high accuracy which limits the radiation effect on the surrounding healthy tissues [138].

The Leksell Gamma Knife is a medical device developed by the company Elekta AB¹⁰ for the treatment of brain tumors. First developed in 1967, the Gamma Knife is based on the concept of radiosurgery. Figure 3.9(a) shows one of the most recent models of the Gamma Knife which is called Perfexion[®] and introduced in 2006 [139]. By aiming Gamma radiation on the tumor cells, the Gamma Knife treats benign and malignant tumors as well as various malfunctions in the brain. It has been proven effective for patients with tumors up to 4 cm in size, vascular malformations such as arteriovenous malformation, pain or other functional problems [140], [141]. Cobalt-60 is the radiation source that is distributed in five circular rings, as shown in Figure 3.9(b), and is heavily shielded by lead, iron, and tungsten to avoid leakage of Gamma radiation. In order for the patient's head to remain stationary and thus to avoid errors from patient movements during the treatment, an aluminum frame is surgically fixed to the skull. When calculating dose, the

¹⁰www.elekta.com/radiosurgery

frame becomes a reference for the coordinate system, hence a stereotactic frame.

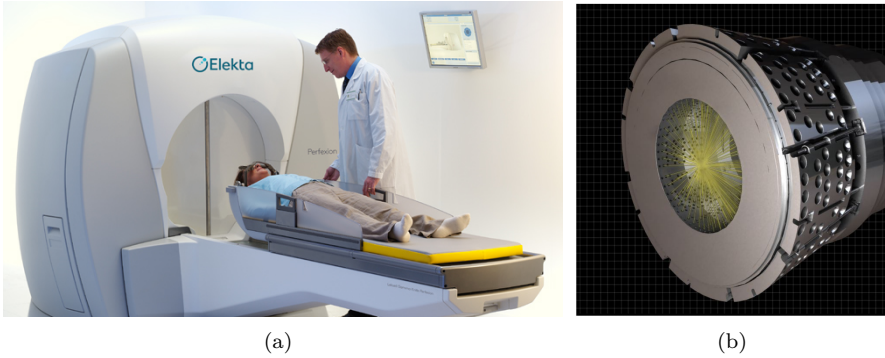


Figure 3.9: (a) The Gamma Knife Perfexion[®] (b) Metallic frame and the conceptual focusing of the rays in Gamma Knife.

Radiobiology

Describing what happens to a cell when irradiated, research in radiobiology contributes to the development of radiotherapy (RT) and radiosurgery (SRS) in three important ways [131]. Firstly, it may provide an extended conceptual basis for RT and SRS by identifying the underlying mechanisms and processes for tumor and normal tissue response to radiation. Examples are knowledge about reoxygenation, hypoxia, and repair of DNA damage. Secondly, it can help in the development of radiotherapy/ radiosurgery treatment plans. Thirdly, using conversion formulas for changes in fractions or dose rate, it can also provide a tool for the patient-specific selection of the best RT or SRS dose schedules.

LQ Model

The Linear Quadratic model, LQ-model, is the most widely used model to estimate cell survival after radiation. According to this model, one can express the surviving fraction (SF) of target cells after receiving the dose per fraction D as follows

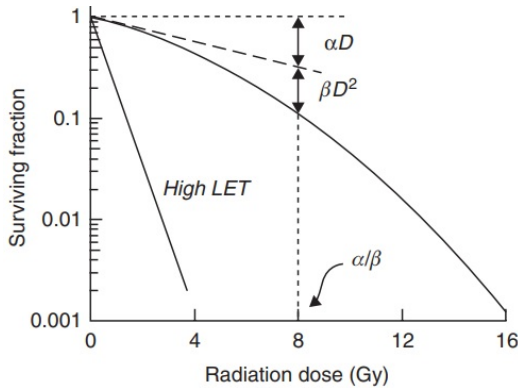


Figure 3.10: Explanatory plot for the linear and quadratic parts of the LQ model (Taken and reprinted from [131]).

$$SF = e^{-\alpha D - \beta D^2} \quad (3.6)$$

where α and β are the parameters coming from a curve-fitting to the survival graphs. As can be seen from the exponent of Equation 3.6, the underlying assumption of this model is that there is a linear and a quadratic component for the exponential cell survival versus dose as demonstrated in Figure 3.10. The α/β ratio is determined when the two portions of αD and βD^2 become equal as shown in the plot ($\alpha/\beta = 8 \text{ Gy}$ in the figure). This ratio describes the bendiness of the cell-survival curve. In other words, a high $\frac{\alpha}{\beta}$ -ratio implies that the tissue is early responding to radiation whereas a low $\frac{\alpha}{\beta}$ -ratio means it takes longer for the tissues to respond to the radiation effect.

Hypoxia

Supply of oxygen has a strong impact on the cell's response to ionizing radiation. In fact, oxygen is a strong radiosensitizer, i.e. it makes the tumors more sensitive to radiation. Tumors may outgrow their blood supply and therefore become hypoxic. Hypoxia is a condition under which cells are far away from the diffusion distance of a blood vessel. These hypoxic tumor cells may be twice or three times as resistant to radiation damage as the cells under normally oxygenated conditions [131]. Using the LQ-model, Figure 3.11 shows

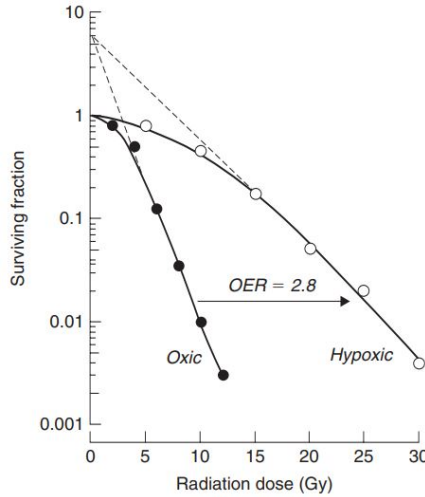


Figure 3.11: Modifying effect of oxygen to the radiation dose: survival curves for cultured mammalian cells exposed to X-rays under oxic and hypoxic conditions. OER stands for Oxygen Enhancement Ratio (Taken and reprinted from [131]).

how the radiation resistance of the cells decreases by a factor of 2.8 from a hypoxic condition to an oxic condition. Having the Oxygen Enhancement Ratio (OER) for a specific tissue at hand, one can modify the α and β parameters in the LQ-model by taking into account the distance to molecular oxygen [142]. The detailed discussion about the Oxygen Modification Factor (OMF) and its calculation is given in *Paper C*.

Thermoradiotherapy

One of the ongoing developments to further improve the quantitative reliability of HTP routines is to formulate a biological model to quantify the radiosensitizing effect of hyperthermia in terms of equivalent radiation dose (EQD). However, due to the multiple interaction mechanisms involved, defining an optimization function with clinical relevance for the combined treatment of HT with radiotherapy (RT) which is commonly called thermoradiotherapy is not straightforward. Several studies [127], [143], [144] have already proposed a radiobiological evaluation scheme based on the linear-quadratic (LQ) model.

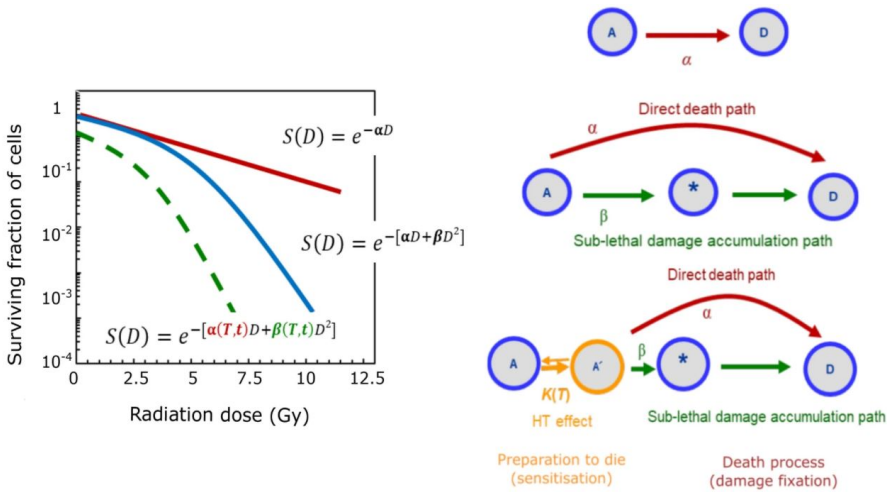


Figure 3.12: Left: Schematic survival probabilities for the three cases depicted on the right. (a) Cell killing as a single rate process with transition rate α from alive (A) to dead (D). (b) Two-step cell killing process in the LQ-model for radiation. A cell transits from the alive state (A) to the dead state (D) through two possible paths: α for direct killing, and β for indirect killing. (c) Combined HT+RT: HT-induced damage elevates cells from state (A) to an activated state (A'), effectively reducing the α/β ratio. (Taken and reprinted from [130]).

They assume temperature-dependent values for the LQ-parameters α and β derived from cervical cell-culture experiments [144].

The cell killing process in thermoradiotherapy is composed of two main stages: sensitization and damage fixation as depicted in Figure 3.12 [130]. As can be seen from the figure, HT-induced damage elevates cells from the 'alive' state to an activated state, thereby effectively reducing the α/β ratio. Since β is efficiently reduced, the direct path α dominates the killing process and consequently reduces the survival probability of tumorous cells [130].

Starting with the well-established, temperature-dependent radiobiological model of LQ, *Paper C* expands the model further by taking into account the oxygenation effects under hypoxic situations in a generic model for brain tumors. The detailed derivation of the model and its parameters are given in *Paper C* and hence are not repeated here. However, the essential points are

highlighted to follow the discussion in this section. Considering the temperature (T), radiation dose (D), the time interval between the two therapies (t_{int}), cell-killing due to direct hyperthermic cytotoxicity (SF_{HT}), and cell-killing due to radiation (SF_{RT}), the overall survival fraction of the combined plan is

$$SF(D, T, t_{int}) = SF_{HT} \times SF_{RT}. \quad (3.7)$$

which also has the oxygenation and fractionation effects (d_{frac}) embedded in its parameters. To find the EQD of the combined plan, the following equation needs to be solved

$$SF(EQD) = SF(D, T, t_{int}) \quad (3.8)$$

and finally the Biological Effective Dose (BED) can to be calculated

$$BED = EQD \times \left(1 + \frac{d_{frac}}{\alpha/\beta}\right). \quad (3.9)$$

When interpreting the equivalent dose predictions, caution should be taken that the predictions are not quantitatively reliable. This is due to uncertainties both in HTP and in the exact values of α - β parameters for different types of tumors and healthy tissues under hyperthermic conditions. Nonetheless, the biological modelling, as demonstrated here, can provide an estimate of the clinical boost of HT in terms of additional radiation dose and the impact of the time interval between RT and HT treatments. Van Leeuwen et al. [127] showed that the application of HT immediately after RT yielded the largest therapeutic gain in the planning phase and confirmed it through a retrospective analysis of clinical data in a follow-up study [126].

In this study, a Stereotactic Radiosurgery (SRS) treatment with Gamma Knife was considered for the RT part. This treatment modality is only performable for small to medium-sized brain tumors. Hence, only the combined plan for case-study 2 which belongs to the child model with a shrunken medulloblastoma tumor is investigated and reported here. The Gamma Knife plan with the prescribed dose of 15 Gy was performed by Elekta AB, Stockholm, Sweden. It resulted in 99.4% coverage and BED of 37.5 Gy when delivered in a single fraction. Given the size of the target, this treatment plan resulted in an unacceptably high V_{10} . In order to mitigate this issue, a five-fraction

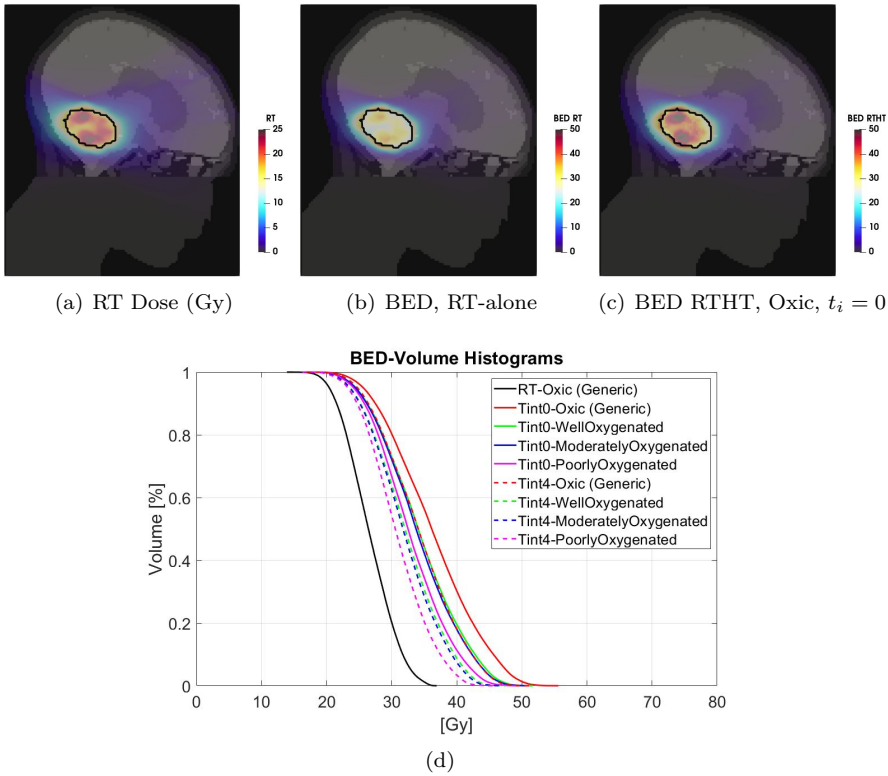


Figure 3.13: Dose and BED distributions in the sagittal plane (a) RT dose distribution (b) BED for the RT plan with the total dose of 15 Gy delivered in five-fractions (c) BED of the combined plan for the oxic tumour and sequential administration, i.e. with the time interval of zero. (d) BED-Volume histograms for the thermoradiotherapy (RTHT) plan.

scheme is considered in the following analysis. Observe that we used a simple, uncompensated scheme where the original treatment dose is maintained despite the fractionation. The Dose distribution of the RT plan is shown in Figure 3.13(a), and the BED distributions (with a different color-bar scale) corresponding to the five-fraction scheme is visualized in Figures 3.13(b) and 3.13(c) for RT-alone and the combined plan, respectively. One can observe a sharp dose gradient around the target that is characteristic of SRS treat-

ments. The boosting effect of adjuvant hyperthermia on the BED is illustrated in Figure 3.13(c) when heat applied to fully oxic tumour directly after irradiation ($t_{int} = 0$). As can be seen, the thermoradiotherapy plan resulted in a substantially higher BED to the Gross Tumor Volume (GTV) than the radiosurgery-only plan.

Figure 3.13(d) summarizes in detail the estimated BED of the combined thermoradiotherapy treatment plan achieved for different oxygenation conditions and sequential administration. The black line represents the results for radiation only, while the coloured lines represent the combined treatment administered with time interval 0 (solid coloured lines) and 4 h after irradiation (dashed coloured lines). Although the results suggest a noticeable increase in the BED values for all levels of oxygenation, the administration of HT directly after RT, that is, $t_{int} = 0$, yields a bigger boost for each oxygenation level. Furthermore, the highest BED is observed for the oxic population, followed by the estimated BED for well-, moderately-, and poorly-oxygenated scenarios.

CHAPTER 4

Microwave Thermometry

As discussed in Chapter 3, the aim of HTP in the pre-treatment optimization stage is to create an accurate treatment plan. Nevertheless, the average literature values for the thermo-dielectric tissue properties, typically used in HTP simulations, and a large intra and inter-patient variation in these parameters make the pre-treatment plan inaccurate. Van de Kamer et al. [145], for instance, have shown that up to 50% uncertainty in dielectric tissue properties can lead to approximately 20% inaccuracy in both SAR and temperature predictions. Moreover, patient movements during a typically one-hour HT treatment cannot be neglected. Therefore, in order to perform a successful HT treatment, a real-time adaptation and re-optimization scheme needs to be integrated into the HTP routine, preferably with thermometry feedback.

Thermometry is an integral part of HT routines to evaluate and control the quality of the clinical outcome. Currently, the invasive method based on fiber optic catheters [146] and the minimally-invasive endoluminal thermometry [147] are the most common types of temperature measurements in clinical HT trials. Due to restrictions on the placement of the catheters/thermal probes, the invasive thermometry provides only limited information about the volumetric temperature distributions. Therefore, to improve the

treatment outcomes and patient's comfort, the growing trend in the field has been towards non-invasive techniques such as magnetic resonance (MR) [148], [149], ultrasound [150], and microwave thermometry. MR-thermometry has been clinically proven as a reliable real-time temperature monitoring technique. It has a high spatial resolution and anatomical coverage per unit time [148], but it is expensive and thus not affordable for all clinical centers. MR is also not suitable for intraoperative monitoring in patients with MR incompatible pacemakers or artificial heart valves.

Microwave-based methods can be classified into two categories: passive sensing approaches such as microwave radiometry [46], [151], [152] and active microwave thermometry (MWT). Microwave radiometry, which is based on Planck's radiation law, measures the thermal electromagnetic radiation emitted by lossy media at temperatures above absolute zero. Active MWT methods, which are based on the illumination of the object under test with EM waves and the analysis of the scattered waves, can further be divided into tomography-based [153]–[155] and UWB radar-based [156] techniques. This chapter proposes an active, tomography-based MWT method and assesses its feasibility for practical implementations.

4.1 The Reconstruction Algorithm

The temperature dependence of dielectric properties of biological tissues ($\Delta\epsilon$, $\Delta\sigma$, or $\Delta O = |\Delta\epsilon_r + \frac{j}{\omega\epsilon_b}\Delta\sigma|$) makes it possible to detect the temperature changes during an HT treatment. The challenges in the hyperthermic mild increase above the normal body temperature ($[4-7]^\circ C$) lie in (a) the detection of small changes in the tissue dielectric properties which are typically less than 1% per $^\circ C$ and (b) in the proper conversion of $\Delta\epsilon$, $\Delta\sigma$, or ΔO into temperature. The magnitude of these dielectric changes in the microwave frequency range depends on the tissue water content. Dielectric spectroscopies on animal tissue [157] show that the high-water content tissue such as muscle and liver, for instance, exhibit larger changes in their dielectric properties during heating while the low-water content tissues such as fat and bone show significantly lower temperature dependencies.

This section summarizes the method in an easy-to-follow pseudo-codes/flowcharts while all the derivations of formulas have been given in *Paper D*.

Least-Square Reconstruction

After discretization of the Region of Interest (RoI) and using the Distorted Born Approximation (DBA) method, the reconstruction problem reduces to a familiar linear algebraic equation which is ill-posed and hence requires a regularization scheme. To solve this problem, Tikhonov functional is defined as follows [158]

$$F(m) = \frac{1}{2} \|Am - d\|_{L_2}^2 + \frac{\lambda}{2} \|m\|_{L_2}^2 \quad (4.1)$$

where A is the discretized linear forward operator; m is the contrast function that relates to the dielectric changes due to temperature and hence is the sought-after unknown in this equation; d is the differential input to the algorithm; and λ is the Tikhonov regularization parameter. Steps taken in the least-square (LS) reconstruction are summarized in Algorithm 1.

Adaptive FEM Refinement

Choosing a proper regularization parameter (λ) is not straightforward and differs from scenario to scenario. In the literature, the balancing principle is proposed for the selection of the optimal λ at each time step. Moreover, through local refinement of the mesh, the quality of the reconstructed images can be improved at the expense of small computational overhead. To this end,

Algorithm 1 LS Reconstruction

- 1: **Base-line scenario at $t = 0$:** Extract both the electric field distribution of the RoI and S-matrix $[S^B]$ from CST.
 - 2: **The time series of S-matrices:** Measure the S-matrices $[S^1], [S^2], \dots, [S^n]$ at temporal steps of $[T_1], [T_2], \dots, [T_n]$
 - 3: **The differential input to the algorithm:** For time step i , calculate the differential input $d^i = [S^B] - [S^i]$ and feed it to the algorithm.
 - 4: **Image reconstruction based on DBA method:** Having the linear forward operator A at hand, form the linear-algebraic equation of $Am^i = d^i$ to find the contrast function m at i -th time step.
 - 5: **Minimization of the Tikhonov functional:** Solve the above mentioned equation through minimization of the Tikhonov functional using the Singular Value Decomposition (SVD) method.
-

an adaptive finite element method (AFEM) [159] was used to refine the mesh and consequently to improve the reconstruction quality. The flowchart of the AFEM algorithm used in *Paper D* is shown in Figure 4.1.

4.2 Proof of Concept – Measurement

Monopole System

To assess the feasibility of the method, an experiment was conducted to monitor the cooling process of a hot object in a 10-minute window of time. A MW imaging system developed in the group for breast cancer detection was used for this feasibility study. It consists of 16 monopole antennas immersed in a mixture of water-glycerin as the matching liquid. Figure 4.2 shows the setup along with the cylindrical inclusion that was filled with hot liquid and subsequently inserted in the tank for monitoring. The measured rate of temperature change in the liquid as well as its dielectric change due to temperature are shown in Figures 4.3(a) and 4.3(b), respectively.

Finally, the reconstructed thermograms of the scenario are shown in Figure 4.4. As can be seen, the LS algorithm was successful in locating where the thermal changes had occurred. However some artifacts are recognizable in the reconstructed profiles, in particular around the plastic container of the target. The AFEM refinement may help to reduce these artifacts to some extent but still remains to be performed in future studies. Also, note that the obtained thermograms are qualitative measures of changes in the contrast function over time. Therefore, in order to be interpreted as a thermometer with a proper scale, they need to be further mapped back to the temperature.

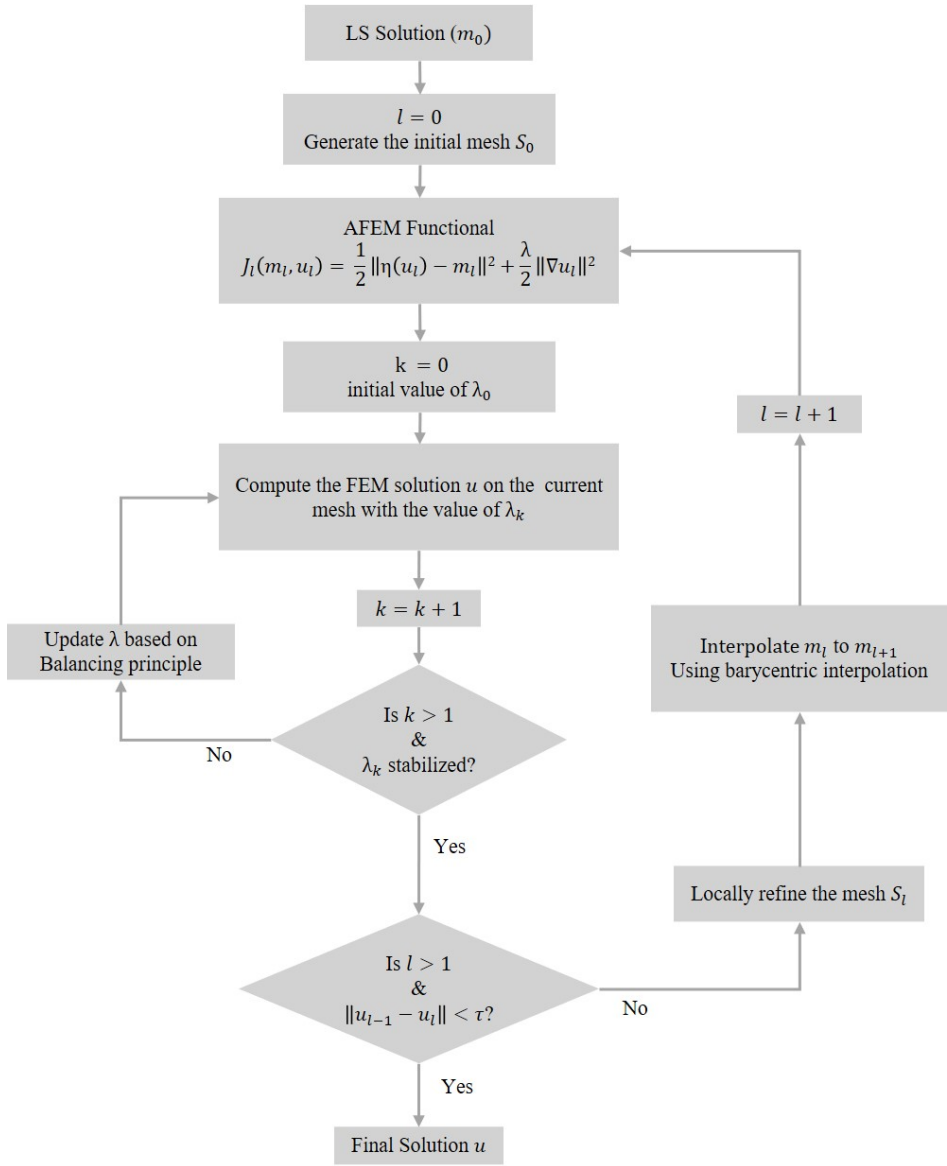


Figure 4.1: Flowchart of the AFEM technique used in Paper D.

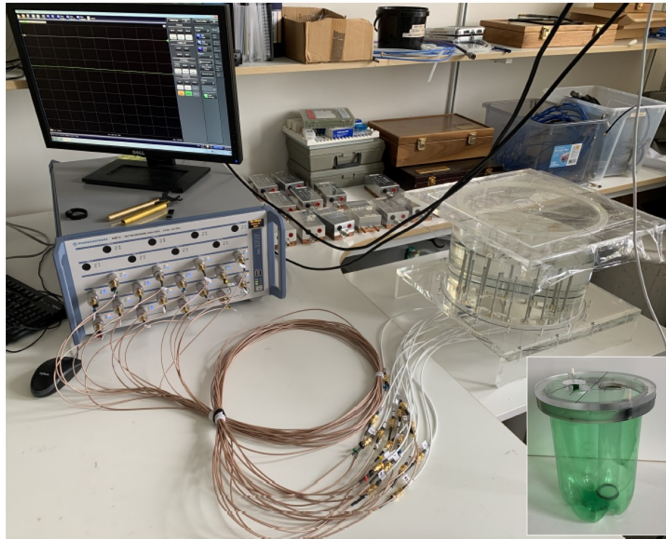


Figure 4.2: The experimental setup for microwave thermometry including an R&S 16-channel VNA and an array of 16 monopole antennas submerged in a tank of matching liquid. The inset shows the cylindrical inclusion that was filled with heated matching liquid.

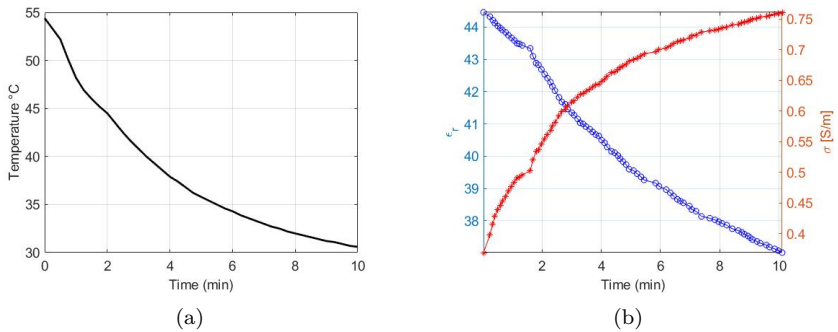


Figure 4.3: Thermal response of the heated matching liquid (a) Its rate of cooling over a course of 10 minutes (b) Its dielectric changes due to cooling in the same window of time.

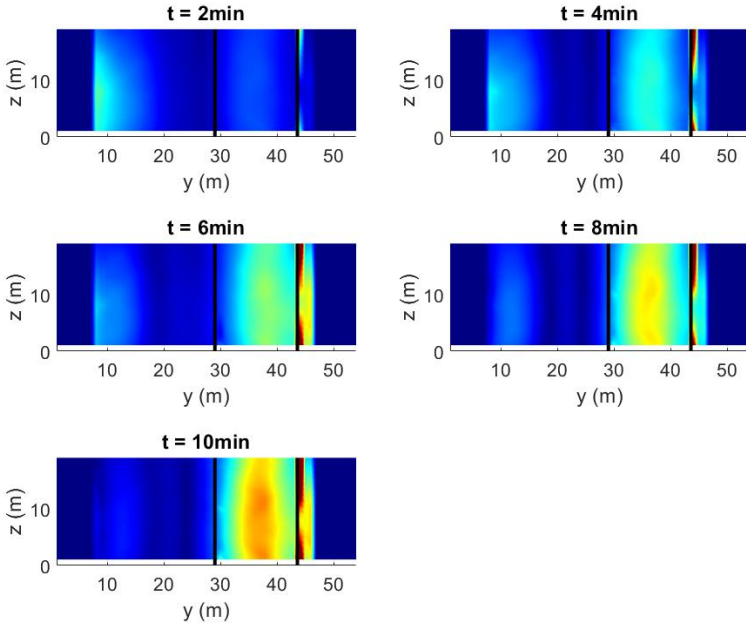


Figure 4.4: Qualitative reconstructions for the heated cylinder. 2D slices in the $Y - Z$ plane with a 2-minute time step show the dielectric changes in the RoI as the target cools down within a period of 10 minutes.

CHAPTER 5

Summary of included papers

This chapter provides a summary of the included papers.

5.1 Paper A

Morteza Ghaderi Aram, Hadi Aliakbarian, Hana Dobšíček Trefná
An ultra-wideband compact design for hyperthermia: Open ridged-waveguide antenna
Published in IET Microwaves, Antennas & Propagation,
Jan. 2022.
©Wiley DOI: 10.1049/mia2.12226.

The focus of Paper A is to design an element of a phased array applicator, i.e. the antenna. Antennas are the building block of applicators whose design and fabrication require special attention to assure an efficient energy transfer. They are loaded with a patient body located not well into their far-field, and for an efficient transition of waves, they demand a matching medium, a water bolus. Important features of a good antenna design for hyperthermic applications are to have a wide frequency band of operation, to be compact and

robust to environmental noise, to have a sufficient penetration depth, and to leave a small EMI footprint.

To introduce a new and efficient antenna element, Paper A proposes a customized antenna design from the double-ridged horn (DRH) family and names it open ridged-waveguide (ORWG). The design procedure starts with a scaled version of a well-established DRH design which is further tailored and optimized to suit the HT applications. The optimized design is fabricated and its performance is assessed both numerically and experimentally according to the HT quality assurance guidelines.

The proposed antenna satisfies all the requirements of the HT guidelines for both superficial and deep hyperthermia. Moreover, the reported results make the design stand out from the previously proposed models in the field by showing that

- The new antenna model has a wide operational bandwidth, with a fractional bandwidth more than 75% from 400 MHz to 800 MHz.
- The antenna needs no balun or RF matching network. Hence the stray losses associated with balun are avoided in this design.
- ORWG is an efficient radiator to deposit energy deeply enough into the body.

5.2 Paper B

Morteza Ghaderi Aram, Hadi Aliakbarian, Hana Dobšiček Trefná
A phased array applicator based on open ridged-waveguide antenna for microwave hyperthermia
Published in Microwave and Optical Technology Letters,
vol. 63, no. 12, pp. 3086-3091, Sep. 2021.
©Wiley DOI: 10.1002/mop.33039.

Paper B is a short communication to demonstrate the feasibility of focusing energy into deep-seated tumors via an elliptical phased array applicator consisting of 16 ORWG antennas. The focus of Paper B is not on the antenna itself but rather on the antenna's function as an element within the phased array applicator, mutual coupling of the adjacent elements, and beamforming for an efficient power deposition. A hybrid, in-house beamforming method

based on time reversal (TR) and particle swarm Optimization (PSO) to avoid getting trapped in local minima and to have a faster convergence is also introduced.

The power deposition capability of the proposed applicator was investigated on a realistic H&N patient model with a relatively large tumor in his tongue. After exporting the power loss densities (PLD) of all 16 antennas simulated in CST, we performed the hybrid TR-PSO beamforming method in Matlab for the treatment planning of the patient model. Thermal simulation of the scenario was subsequently performed by FEniCS, an open-source FEM-based computational platform.

The effectiveness of the proposed applicator, the beamforming method, and the ensuing thermal analysis was quantitatively assessed by the calculation of SAR-based and temperature-based quality metrics such as target coverage 25% ($TC_{25\%}$), T_{90} , T_{50} , and T_{10} . Overall, satisfactory results of this short letter motivate fabrication of the proposed applicator for future studies and eventually for clinical trials.

5.3 Paper C

Morteza Ghaderi Aram, Massimiliano Zanoli, Håkan Nordström, Iuliana Toma-Dasu, Klas Blomgren, Hana Dobšiček Trefná

Radiobiological Evaluation of Combined Gamma Knife Radiosurgery and Hyperthermia for Pediatric Neuro-Oncology

Published in Cancers,

vol. 13, no. 13, pp. 3277, Jun. 2021.

©MDPI DOI: 10.3390/cancers13133277.

Paper C investigates the radiobiological modeling of a synergistic cancer treatment modality in which the Gamma Knife stereotactic radiosurgery (SRS) is combined with hyperthermia. Previous studies have shown the enhancement brought about by the addition of HT to the traditional cancer treatment modalities. These studies are mainly concerned with gliomas in adolescents treated with external beam radiotherapy (EBRT). However, the combination of the Gamma knife radiosurgery with intracranial focused heating in pediatrics has never been assessed before.

Incorporating the oxygenation effect, we expanded a well-established radiobiological model, better known as the linear-quadratic (LQ) model. The model

was then used for a challenging medulloblastoma treatment to assess how HT could boost the therapeutic outcomes for two different time intervals between the two therapies. The results were examined by different quality metrics: biologically effective dose (BED) and tumor control probability (TCP). Although the effect of time interval on the TCP assessed in this study is not very noticeable, the highest gain is expected through a sequential application of HT after RT, i.e. with the time interval of 0. Furthermore, the results indicate that HT can considerably boost the BED delivered to the GTV. Alternatively, one can conclude that for the same therapeutic effect of a fractionated RT-alone treatment, HT can help reduce the amount of dose delivered undesirably to the healthy tissue. This motivates further development of HT devices for such a combined treatment in pediatric neuro-oncology.

5.4 Paper D

Morteza Ghaderi Aram, Larisa Beilina, Hana Dobšiček Trefná
Microwave thermometry with potential application in non-invasive monitoring of hyperthermia

Published in Journal of Inverse and Ill-posed Problems,
vol. 28, no. 5, pp. 739–750, Oct. 2020.

©De Gruyter DOI: 10.1515/jiip-2020-0102 .

This feasibility study investigated the possibility of thermal monitoring of a cooling process through using a differential inverse scattering technique. The underlying assumption is that the thermal changes within the HT range (35–45°C) lead to a tangible change in the dielectric properties of tissues that can then be detected with microwave imaging techniques.

To prove the concept and to improve the reconstruction quality of previously proposed methods in the field, we first explained the simulation details of a simple scenario with 16 monopole antennas circularly arranged in a tank filled with matching liquid. Using a least-square (LS) inversion scheme, we formulated the differential image reconstruction algorithm. Finally, a further step was taken to improve the image quality by hiring an adaptive FEM-based (AFEM) inversion scheme.

Results of the study indicate a successful reconstruction and show that AFEM has the potential to considerably improve the qualitative shape reconstruction of the LS method. The image restoration was achieved through iterative re-

finement of triangular meshes in 2D slices around the regions with a high gradient of functional. This encourages further studies of the subject for realistic patient models that are treated with HT applicators made of more sophisticated antenna elements. Implementation of a full 3D AFEM reconstruction, as well as the development of a mapping scheme to convert the indicator and to correlate it back to temperature, are remaining to be done in future studies.

CHAPTER 6

Concluding Remarks

This report discusses different aspects of microwave hyperthermia, ranging from antenna and applicator designs to microwave thermometry. It proposes a new antenna design whose performance assessments show that the design has a high potential to serve as an element for both phased array and superficial applicators. The MR compatibility of the design, however, remains to be investigated in future studies. Based on this design, a conventional phased array applicator consisting of 16 ORWG antennas arranged in two elliptical rings is proposed and analyzed in the treatment planning of two realistic models. Both the characteristics of the antenna and the quality metrics of the treatment plans are promising which motivates further development and implementation of the proposed applicator.

The treatment planning stage is further enriched by a radiobiological modelling that allows for the evaluation of RTHT combined treatment plans. Using an extended version of the LQ model which has an oxygen modification factor to account for hypoxic conditions in GTV, radiosensitization has been modeled and the results are presented in terms of clinically relevant parameters such as BED and TCP. Treatment monitoring aspects of HT are finally assessed in a feasibility study that investigates the practicality of using the same

microwave system for both heating and monitoring purposes. To this end, an adaptive algorithm is proposed and tested both on simulated and measured data for a monopole-based system. The reconstructions are encouraging and hence motivate further studies. The use of a more dedicated and more sophisticated hyperthermic system instead of the monopole system also remains to be considered in the future.

References

- [1] *National cancer institute, NIH*, <https://www.cancer.gov/>, Accessed: 2021-07-29.
- [2] *American cancer society*, <https://www.cancer.org/>, Accessed: 2021-07-29.
- [3] S. B. Field and C. Franconi, *Physics and technology of hyperthermia*. Springer Science & Business Media, 2012, vol. 127.
- [4] W. H. Organization *et al.*, *The global burden of disease: 2004 update*. World Health Organization, 2008.
- [5] J. Ferlay, H.-R. Shin, F. Bray, D. Forman, C. Mathers, and D. M. Parkin, “Estimates of worldwide burden of cancer in 2008: Globocan 2008,” *International journal of cancer*, vol. 127, no. 12, pp. 2893–2917, 2010.
- [6] A. K. Chaturvedi, W. F. Anderson, J. Lortet-Tieulent, M. P. Curado, J. Ferlay, S. Franceschi, P. S. Rosenberg, F. Bray, and M. L. Gillison, “Worldwide trends in incidence rates for oral cavity and oropharyngeal cancers,” *Journal of clinical oncology*, vol. 31, no. 36, p. 4550, 2013.
- [7] *Global cancer observatory*, <https://gco.iarc.fr/>, Accessed: 2021-08-1.
- [8] H. Sung, J. Ferlay, R. L. Siegel, M. Laversanne, I. Soerjomataram, A. Jemal, and F. Bray, “Global cancer statistics 2020: Globocan estimates of incidence and mortality worldwide for 36 cancers in 185 countries,” *CA: a cancer journal for clinicians*, vol. 71, no. 3, pp. 209–249, 2021.

- [9] *The swedish head and neck cancer register (swehncr)*, <https://www.cancercentrum.se/samverkan/>, Accessed: 2021-07-29.
- [10] D. W. Ellison, "Childhood medulloblastoma: Novel approaches to the classification of a heterogeneous disease," *Acta neuropathologica*, vol. 120, no. 3, pp. 305–316, 2010.
- [11] D. N. Korones, "Treatment of newly diagnosed diffuse brain stem gliomas in children: In search of the holy grail," *Expert review of anticancer therapy*, vol. 7, no. 5, pp. 663–674, 2007.
- [12] S. Uday, R. D. Murray, S. Picton, P. Chumas, M. Raju, M. Chandwani, and S. Alvi, "Endocrine sequelae beyond 10 years in survivors of medulloblastoma," *Clinical endocrinology*, vol. 83, no. 5, pp. 663–670, 2015.
- [13] R. L. Mulder, L. C. Kremer, H. M. van Santen, J. L. Ket, A. P. van Trotsenburg, C. C. Koning, A. Y. Schouten-van Meeteren, H. N. Caron, S. J. Neggers, and E. C. van Dalen, "Prevalence and risk factors of radiation-induced growth hormone deficiency in childhood cancer survivors: A systematic review," *Cancer treatment reviews*, vol. 35, no. 7, pp. 616–632, 2009.
- [14] P. K. Duffner, "Long-term effects of radiation therapy on cognitive and endocrine function in children with leukemia and brain tumors," *The neurologist*, vol. 10, no. 6, pp. 293–310, 2004.
- [15] J. C. Peeken, P. Vaupel, and S. E. Combs, "Integrating hyperthermia into modern radiation oncology: What evidence is necessary?" *Frontiers in oncology*, vol. 7, p. 132, 2017.
- [16] P. B. Elming, B. S. Sørensen, A. L. Oei, N. A. Franken, J. Crezee, J. Overgaard, and M. R. Horsman, "Hyperthermia: The optimal treatment to overcome radiation resistant hypoxia," *Cancers*, vol. 11, no. 1, p. 60, 2019.
- [17] M. W. Dewhirst and T. W. Secomb, "Transport of drugs from blood vessels to tumour tissue," *Nature Reviews Cancer*, vol. 17, no. 12, pp. 738–750, 2017.
- [18] B. F. Jordan and P. Sonveaux, "Targeting tumor perfusion and oxygenation to improve the outcome of anticancer therapy1," *Frontiers in pharmacology*, vol. 3, p. 94, 2012.

-
- [19] A. Oei, H. Kok, S. Oei, M. Horsman, L. Stalpers, N. Franken, and J. Crezee, "Molecular and biological rationale of hyperthermia as radio- and chemosensitizer," *Advanced drug delivery reviews*, vol. 163, pp. 84–97, 2020.
- [20] H. H. Kampinga, "Cell biological effects of hyperthermia alone or combined with radiation or drugs: A short introduction to newcomers in the field," *International journal of hyperthermia*, vol. 22, no. 3, pp. 191–196, 2006.
- [21] N. Datta, S. G. Ordóñez, U. Gaipl, M. Paulides, H. Crezee, J. Gellermann, D. Marder, E. Puric, and S. Bodis, "Local hyperthermia combined with radiotherapy and/or chemotherapy: Recent advances and promises for the future," *Cancer treatment reviews*, vol. 41, no. 9, pp. 742–753, 2015.
- [22] H. Kok and J. Crezee, "Hyperthermia treatment planning: Clinical application and ongoing developments," *IEEE Journal of Electromagnetics, RF and Microwaves in Medicine and Biology*, 2020.
- [23] J. van der Zee, D. González, G. C. van Rhoon, J. D. van Dijk, W. L. van Putten, A. A. Hart, *et al.*, "Comparison of radiotherapy alone with radiotherapy plus hyperthermia in locally advanced pelvic tumours: A prospective, randomised, multicentre trial," *The Lancet*, vol. 355, no. 9210, pp. 1119–1125, 2000.
- [24] R. Colombo, A. Salonia, Z. Leib, M. Pavone-Macaluso, and D. Engelstein, "Long-term outcomes of a randomized controlled trial comparing thermochemotherapy with mitomycin-c alone as adjuvant treatment for non-muscle-invasive bladder cancer (nmibc)," *BJU International-British Journal of Urology*, vol. 107, no. 6, p. 912, 2011.
- [25] N. G. Huilgol, S. Gupta, C. Sridhar, *et al.*, "Hyperthermia with radiation in the treatment of locally advanced head and neck cancer: A report of randomized trial," *Journal of cancer research and therapeutics*, vol. 6, no. 4, p. 492, 2010.
- [26] I. C. H. Group, C. C. Vernon, J. W. Hand, S. B. Field, D. Machin, J. B. Whaley, J. van der Zee, W. L. van Putten, G. C. van Rhoon, J. D. van Dijk, *et al.*, "Radiotherapy with or without hyperthermia in the treatment of superficial localized breast cancer: Results from

- five randomized controlled trials,” *International Journal of Radiation Oncology* Biology* Physics*, vol. 35, no. 4, pp. 731–744, 1996.
- [27] J. Overgaard, S. Bentzen, D. G. Gonzalez, M. Hulshof, G. Arcangeli, O. Dahl, and O. Mella, “Randomised trial of hyperthermia as adjuvant to radiotherapy for recurrent or metastatic malignant melanoma,” *The Lancet*, vol. 345, no. 8949, pp. 540–543, 1995.
- [28] P. Turner, A. Tumeh, and T. Schaefermeyer, “Bsd-2000 approach for deep local and regional hyperthermia: Physics and technology.,” *Strahlentherapie und Onkologie: Organ der Deutschen Rontgengesellschaft...[et al]*, vol. 165, no. 10, pp. 738–741, 1989.
- [29] M. Paulides, J. Bakker, E. Neufeld, J. v. d. Zee, P. Jansen, P. Levendag, and G. Van Rhoon, “The hypercollar: A novel applicator for hyperthermia in the head and neck,” *International Journal of Hyperthermia*, vol. 23, no. 7, pp. 567–576, 2007.
- [30] J. Jagannathan, N. T. Sanghvi, L. A. Crum, C.-P. Yen, R. Medel, A. S. Dumont, J. P. Sheehan, L. Steiner, F. Jolesz, and N. F. Kassell, “High-intensity focused ultrasound surgery of the brain: Part 1—a historical perspective with modern applications,” *Neurosurgery*, vol. 64, no. 2, pp. 201–211, 2009.
- [31] G. R. Giammalva, C. Gagliardo, S. Marrone, F. Paolini, R. M. Gerardi, G. E. Umana, K. Yağmurlu, B. Chaurasia, G. Scalia, F. Midiri, *et al.*, “Focused ultrasound in neuroscience. state of the art and future perspectives,” *Brain sciences*, vol. 11, no. 1, p. 84, 2021.
- [32] B. Behnia, M. Suthar, and A. Webb, “Closed-loop feedback control of phased-array microwave heating using thermal measurements from magnetic resonance imaging,” *Concepts in Magnetic Resonance: An Educational Journal*, vol. 15, no. 1, pp. 101–110, 2002.
- [33] D. K. Cheng *et al.*, *Field and wave electromagnetics*. Pearson Education India, 1989.
- [34] S. Gabriel, R. Lau, and C. Gabriel, “The dielectric properties of biological tissues: Iii. parametric models for the dielectric spectrum of tissues,” *Physics in medicine & biology*, vol. 41, no. 11, p. 2271, 1996.
- [35] E. H. Wissler, “Pennes’ 1948 paper revisited,” *Journal of applied physiology*, vol. 85, no. 1, pp. 35–41, 1998.

-
- [36] J. W. Hand, K. Hynynen, P. Shrivastava, and T. Saylor, *Methods of external hyperthermic heating*. Springer Science & Business Media, 2012.
- [37] J. F. Bakker, M. M. Paulides, A. Westra, H. Schippers, and G. Van Rhoon, “Design and test of a 434 mhz multi-channel amplifier system for targeted hyperthermia applicators,” *International journal of hyperthermia*, vol. 26, no. 2, pp. 158–170, 2010.
- [38] H. Han, T. W. Eigentler, S. Wang, E. Kretov, L. Winter, W. Hoffmann, E. Grass, and T. Niendorf, “Design, implementation, evaluation and application of a 32-channel radio frequency signal generator for thermal magnetic resonance based anti-cancer treatment,” *Cancers*, vol. 12, no. 7, p. 1720, 2020.
- [39] E. Oberacker, A. Kuehne, C. Oezerdem, J. Nadobny, M. Weihrauch, M. Beck, S. Zschaecck, C. Diesch, T. W. Eigentler, H. Waiczies, *et al.*, “Radiofrequency applicator concepts for thermal magnetic resonance of brain tumors at 297 mhz (7.0 tesla),” *International Journal of Hyperthermia*, vol. 37, no. 1, pp. 549–563, 2020.
- [40] E. Oberacker, C. Diesch, J. Nadobny, A. Kuehne, P. Wust, P. Ghadjjar, and T. Niendorf, “Patient-specific planning for thermal magnetic resonance of glioblastoma multiforme,” *Cancers*, vol. 13, no. 8, p. 1867, 2021.
- [41] I. VilasBoas-Ribeiro, S. Curto, G. C. van Rhoon, M. Franckena, and M. M. Paulides, “Mr thermometry accuracy and prospective imaging-based patient selection in mr-guided hyperthermia treatment for locally advanced cervical cancer,” *Cancers*, vol. 13, no. 14, p. 3503, 2021.
- [42] M. Paulides, H. D. Trefna, S. Curto, and D. Rodrigues, “Recent technological advancements in radiofrequency-andmicrowave-mediated hyperthermia for enhancing drug delivery,” *Advanced drug delivery reviews*, vol. 163, pp. 3–18, 2020.
- [43] G. Cappiello, “Towards improved treatment planning for head and neck microwave hyperthermia,” Ph.D. dissertation, NUI Galway, 2019.
- [44] G. Van Rhoon, P. Rietveld, and J. Van der Zee, “A 433 mhz lucite cone waveguide applicator for superficial hyperthermia,” *International journal of hyperthermia*, vol. 14, no. 1, pp. 13–27, 1998.

- [45] M. de Bruijne, J. Van der Zee, A. Ameziane, and G. C. Van Rhoon, "Quality control of superficial hyperthermia by treatment evaluation," *International Journal of Hyperthermia*, vol. 27, no. 3, pp. 199–213, 2011.
- [46] S. Jacobsen, P. R. Stauffer, and D. G. Neuman, "Dual-mode antenna design for microwave heating and noninvasive thermometry of superficial tissue disease," *IEEE Transactions on Biomedical Engineering*, vol. 47, no. 11, pp. 1500–1509, 2000.
- [47] P. Wust, B. Hildebrandt, G. Sreenivasa, B. Rau, J. Gellermann, H. Riess, R. Felix, and P. Schlag, "Hyperthermia in combined treatment of cancer," *The lancet oncology*, vol. 3, no. 8, pp. 487–497, 2002.
- [48] P. Rietveld, M. Lumori, J. van der Zee, and G. Van Rhoon, "Quantitative evaluation of arrays of lucite cone applicators in flat layered phantoms using gaussian-beam-predicted and thermographically measured sar distributions," *Physics in Medicine & Biology*, vol. 43, no. 8, p. 2207, 1998.
- [49] P. R. Stauffer, P. Maccarini, K. Arunachalam, O. Craciunescu, C. Diederich, T. Juang, F. Rossetto, J. Schlorff, A. Milligan, J. Hsu, *et al.*, "Conformal microwave array (cma) applicators for hyperthermia of diffuse chest wall recurrence," *International Journal of Hyperthermia*, vol. 26, no. 7, pp. 686–698, 2010.
- [50] E. A. Gelvich and V. N. Mazokhin, "Contact flexible microstrip applicators (cfma) in a range from microwaves up to short waves," *IEEE Transactions on Biomedical Engineering*, vol. 49, no. 9, pp. 1015–1023, 2002.
- [51] H. P. Kok, M. De Greef, D. Correia, P. J. Zum Vörde Sive Vörding, G. Van Stam, E. A. Gelvich, A. Bel, and J. Crezee, "FDTD simulations to assess the performance of cfma-434 applicators for superficial hyperthermia," *International Journal of Hyperthermia*, vol. 25, no. 6, pp. 462–476, 2009.
- [52] J. Johnson, D. Neuman, P. Maccarini, T. Juang, P. Stauffer, and P. Turner, "Evaluation of a dual-arm archimedean spiral array for microwave hyperthermia," *International Journal of Hyperthermia*, vol. 22, no. 6, pp. 475–490, 2006.

-
- [53] N. R. Datta, E. Puric, J. Heüberger, D. Marder, N. Lomax, O. Timm, P. Memminger, and S. Bodis, “Hyperthermia and reirradiation for locoregional recurrences in preirradiated breast cancers: A single institutional experience,” *Swiss medical weekly*, vol. 145, w14133, 2015.
- [54] J. Crezee, G. Van Tienhoven, M. W. Kolff, J. Sijbrands, G. Van Stam, S. Oldenburg, E. D. Geijssen, M. C. Hulshof, and H. P. Kok, “Development of a 70 mhz unit for hyperthermia treatment of deep-seated breast tumors,” *International Journal of Microwave and Wireless Technologies*, vol. 9, no. 6, pp. 1317–1324, 2017.
- [55] J. Crezee, P. Van Haaren, H. Westendorp, M. De Greef, H. Kok, J. Wiersma, G. Van Stam, J. Sijbrands, P. Zum Vörde Sive Vörding, J. Van Dijk, *et al.*, “Improving locoregional hyperthermia delivery using the 3-d controlled amc-8 phased array hyperthermia system: A pre-clinical study,” *International Journal of Hyperthermia*, vol. 25, no. 7, pp. 581–592, 2009.
- [56] A. A. De Leeuw and J. J. Lagendijk, “Design of a clinical deep-body hyperthermia system based on the ‘coaxial tem’ applicator,” *International journal of hyperthermia*, vol. 3, no. 5, pp. 413–421, 1987.
- [57] P. Raskmark, S. N. Hornsleth, L. N. Salling, J. C. Lindegaard, and J. Overgaard, “Deep heating using a movable applicator phased array hyperthermia system: A preclinical feasibility study,” *Acta Oncologica*, vol. 33, no. 4, pp. 451–455, 1994.
- [58] P. Togni, Z. Rijnen, W. Numan, R. Verhaart, J. Bakker, G. Van Rhooon, and M. Paulides, “Electromagnetic redesign of the hypercollar applicator: Toward improved deep local head-and-neck hyperthermia,” *Physics in Medicine & Biology*, vol. 58, no. 17, p. 5997, 2013.
- [59] M. M. Paulides, P. R. Stauffer, E. Neufeld, P. F. Maccarini, A. Kyr-iakou, R. A. Canters, C. J. Diederich, J. F. Bakker, and G. C. Van Rhooon, “Simulation techniques in hyperthermia treatment planning,” *International Journal of Hyperthermia*, vol. 29, no. 4, pp. 346–357, 2013.
- [60] H. Kok, P. Wust, P. R. Stauffer, F. Bardati, G. Van Rhooon, and J. Crezee, “Current state of the art of regional hyperthermia treatment planning: A review,” *Radiation Oncology*, vol. 10, no. 1, pp. 1–14, 2015.

- [61] M. Paulides, Z. Rijnen, P. Togni, R. Verhaart, T. Drizdal, D. De Jong, M. Franckena, G. Verduijn, and G. Van Rhoon, "Clinical introduction of novel microwave hyperthermia technology: The hypercollar3d applicator for head and neck hyperthermia," in *2015 9th European Conference on Antennas and Propagation (EuCAP)*, IEEE, 2015, pp. 1–4.
- [62] P. Takook, M. Shafiemehr, M. Persson, and H. D. Trefná, "Experimental evaluation of uwb applicator prototype for head and neck hyperthermia," in *2017 11th European Conference on Antennas and Propagation (EuCAP)*, IEEE, 2017, pp. 3619–3620.
- [63] M. Paulides, J. Bakker, M. Linthorst, J. Van der Zee, Z. Rijnen, E. Neufeld, P. Pattynama, P. Jansen, P. Levendag, and G. Van Rhoon, "The clinical feasibility of deep hyperthermia treatment in the head and neck: New challenges for positioning and temperature measurement," *Physics in Medicine & Biology*, vol. 55, no. 9, p. 2465, 2010.
- [64] Z. Rijnen, P. Togni, R. Roskam, S. G. Van De Geer, R. H. Goossens, and M. M. Paulides, "Quality and comfort in head and neck hyperthermia: A redesign according to clinical experience and simulation studies," *International Journal of Hyperthermia*, vol. 31, no. 8, pp. 823–830, 2015.
- [65] P. Takook, M. Persson, J. Gellermann, and H. D. Trefná, "Compact self-grounded bow-tie antenna design for an uwb phased-array hyperthermia applicator," *International Journal of Hyperthermia*, vol. 33, no. 4, pp. 387–400, 2017.
- [66] S. Curto, "Antenna development for radio frequency hyperthermia applications," 2010.
- [67] C. H. Durney and M. F. Iskander, "Antennas for medical applications," in *Antenna Handbook*, Springer, 1993, pp. 596–654.
- [68] M. M. Paulides, J. F. Bakker, N. Chavannes, and G. C. Van Rhoon, "A patch antenna design for application in a phased-array head and neck hyperthermia applicator," *IEEE Transactions on Biomedical Engineering*, vol. 54, no. 11, pp. 2057–2063, 2007.

-
- [69] L. Winter, C. Özerdem, W. Hoffmann, D. Santoro, A. Müller, H. Waiczies, R. Seemann, A. Graessl, P. Wust, and T. Niendorf, “Design and evaluation of a hybrid radiofrequency applicator for magnetic resonance imaging and rf induced hyperthermia: Electromagnetic field simulations up to 14.0 tesla and proof-of-concept at 7.0 tesla,” *PLoS one*, vol. 8, no. 4, e61661, 2013.
- [70] M. Paulides, R. Mestrom, G. Salim, B. Adela, W. Numan, T. Drizdal, D. Yeo, and A. Smolders, “A printed yagi–uda antenna for application in magnetic resonance thermometry guided microwave hyperthermia applicators,” *Physics in Medicine & Biology*, vol. 62, no. 5, p. 1831, 2017.
- [71] P. Turner, A. Tumeh, and T. Schaefermeyer, “Bsd-2000 approach for deep local and regional hyperthermia: Physics and technology.,” *Strahlentherapie und Onkologie: Organ der Deutschen Röntgengesellschaft...[et al]*, vol. 165, no. 10, pp. 738–741, 1989.
- [72] D. Fatehi and G. C. Van Rhoon, “Sar characteristics of the sigma-60-ellipse applicator,” *International journal of hyperthermia*, vol. 24, no. 4, pp. 347–356, 2008.
- [73] R. Zweije, H. P. Kok, A. Bakker, A. Bel, and J. Crezee, “Technical and clinical evaluation of the alba-4d 70mhz loco-regional hyperthermia system,” in *2018 48th European Microwave Conference (EuMC)*, IEEE, 2018, pp. 328–331.
- [74] J. Yang and A. Kishk, “A novel low-profile compact directional ultra-wideband antenna: The self-grounded bow-tie antenna,” *IEEE Transactions on Antennas and Propagation*, vol. 60, no. 3, pp. 1214–1220, 2011.
- [75] A. Kazemipour and X. Begaud, “Calculable dipole antenna for emc measurements with low-loss wide-band balun from 30 mhz to 2 ghz,” *Electromagnetics*, vol. 25, no. 3, pp. 187–202, 2005.
- [76] R. E. Collin, *Field theory of guided waves*. John Wiley & Sons, 1990, vol. 5.
- [77] S. B. Cohn, “Properties of ridge wave guide,” *Proceedings of the IRE*, vol. 35, no. 8, pp. 783–788, 1947.

- [78] S. Hopfer, “The design of ridged waveguides,” *IRE Transactions on Microwave Theory and Techniques*, vol. 3, no. 5, pp. 20–29, 1955.
- [79] W. Sun and C. A. Balanis, “Mfie analysis and design of ridged waveguides,” *IEEE Transactions on Microwave theory and Techniques*, vol. 41, no. 11, pp. 1965–1971, 1993.
- [80] D. O. Rodriguez-Duarte, J. A. T. Vasquez, R. Scapatucci, L. Crocco, and F. Vipiana, “Brick-shaped antenna module for microwave brain imaging systems,” *IEEE Antennas and Wireless Propagation Letters*, vol. 19, no. 12, pp. 2057–2061, 2020.
- [81] A. R. Mallahzadeh and A. Imani, “Double-ridged antenna for wideband applications,” *Progress In Electromagnetics Research*, vol. 91, pp. 273–285, 2009.
- [82] H. D. Trefná, J. Crezee, M. Schmidt, D. Marder, U. Lamprecht, M. Ehmann, J. Nadobny, J. Hartmann, N. Lomax, S. Abdel-Rahman, *et al.*, “Quality assurance guidelines for superficial hyperthermia clinical trials,” *Strahlentherapie und Onkologie*, vol. 193, no. 5, pp. 351–366, 2017.
- [83] H. D. Trefná, H. Crezee, M. Schmidt, D. Marder, U. Lamprecht, M. Ehmann, J. Hartmann, J. Nadobny, J. Gellermann, N. van Holthe, *et al.*, “Quality assurance guidelines for superficial hyperthermia clinical trials: I. clinical requirements,” *International Journal of Hyperthermia*, vol. 33, no. 4, pp. 471–482, 2017.
- [84] H. D. Trefná and A. Ström, “Hydrogels as a water bolus during hyperthermia treatment,” *Physics in Medicine & Biology*, vol. 64, no. 11, p. 115025, 2019.
- [85] J. Lee and S. Nam, “Effective area of a receiving antenna in a lossy medium,” *IEEE transactions on antennas and propagation*, vol. 57, no. 6, pp. 1843–1845, 2009.
- [86] S. M. Aguilar, M. A. Al-Joumayly, M. J. Burfeindt, N. Behdad, and S. C. Hagness, “Multiband miniaturized patch antennas for a compact, shielded microwave breast imaging array,” *IEEE transactions on antennas and propagation*, vol. 62, no. 3, pp. 1221–1231, 2013.

-
- [87] G. Bruggmoser, S. Bauchowitz, R. Canters, H. Crezee, M. Ehmann, J. Gellermann, U. Lamprecht, N. Lomax, M. Messmer, O. Ott, *et al.*, “Guideline for the clinical application, documentation and analysis of clinical studies for regional deep hyperthermia,” *Strahlentherapie und Onkologie*, vol. 188, no. 2, pp. 198–211, 2012.
- [88] M. M. Paulides, S. H. Vossen, A. P. Zwamborn, and G. C. van Rhoon, “Theoretical investigation into the feasibility to deposit rf energy centrally in the head-and-neck region,” *International Journal of Radiation Oncology* Biology* Physics*, vol. 63, no. 2, pp. 634–642, 2005.
- [89] *Tissue properties database. v3.1. 2016*, <http://itis.swiss/virtual-population/tissue-properties/downloads-v3-1/>, Accessed: 2021-07-29.
- [90] A. Christ, W. Kainz, E. G. Hahn, K. Honegger, M. Zefferer, E. Neufeld, W. Rascher, R. Janka, W. Bautz, J. Chen, *et al.*, “The virtual family—development of surface-based anatomical models of two adults and two children for dosimetric simulations,” *Physics in Medicine & Biology*, vol. 55, no. 2, N23, 2009.
- [91] M.-C. Gosselin, E. Neufeld, H. Moser, E. Huber, S. Farcito, L. Gerber, M. Jedensjö, I. Hilber, F. Di Gennaro, B. Lloyd, *et al.*, “Development of a new generation of high-resolution anatomical models for medical device evaluation: The virtual population 3.0,” *Physics in Medicine & Biology*, vol. 59, no. 18, p. 5287, 2014.
- [92] S. N. Makarov, G. M. Noetscher, J. Yanamadala, M. W. Piazza, S. Louie, A. Prokop, A. Nazarian, and A. Nummenmaa, “Virtual human models for electromagnetic studies and their applications,” *IEEE reviews in biomedical engineering*, vol. 10, pp. 95–121, 2017.
- [93] T. Rylander, P. Ingelström, and A. Bondeson, *Computational electromagnetics*. Springer Science & Business Media, 2012.
- [94] K. Yee, “Numerical solution of initial boundary value problems involving maxwell’s equations in isotropic media,” *IEEE Transactions on antennas and propagation*, vol. 14, no. 3, pp. 302–307, 1966.
- [95] A. Taflove and S. Hagness, “Computational electrodynamics: The finite-difference time-domain method 3rd edn (norwood, ma: Artech house),” *Wiley*, 2005.

- [96] M. Clemens and T. Weiland, “Discrete electromagnetism with the finite integration technique,” *Progress In Electromagnetics Research*, vol. 32, pp. 65–87, 2001.
- [97] T. Weiland, M. Timm, and I. Munteanu, “A practical guide to 3-d simulation,” *IEEE Microwave Magazine*, vol. 9, no. 6, pp. 62–75, 2008.
- [98] M. Kozlov and R. Turner, “A comparison of ansoft hfss and cst microwave studio simulation software for multi-channel coil design and sar estimation at 7t mri,” *Piers online*, vol. 6, no. 4, pp. 395–399, 2010.
- [99] V. Dolean, H. Fahs, L. Fezoui, and S. Lanteri, “Locally implicit discontinuous galerkin method for time domain electromagnetics,” *Journal of Computational Physics*, vol. 229, no. 2, pp. 512–526, 2010.
- [100] H. Kok, P. Van Haaren, J. Van de Kamer, J. Wiersma, J. Van Dijk, and J. Crezee, “High-resolution temperature-based optimization for hyperthermia treatment planning,” *Physics in Medicine & Biology*, vol. 50, no. 13, p. 3127, 2005.
- [101] R. Canters, M. Paulides, M. Franckena, J. Mens, and G. Van Rhoon, *Benefit of replacing the sigma-60 by the sigma-eye applicator*, 2013.
- [102] H. K. Lee, A. G. Antell, C. A. Perez, W. L. Straube, G. Ramachandran, R. J. Myerson, B. Emami, E. P. Molmenti, A. Buckner, and M. A. Lockett, “Superficial hyperthermia and irradiation for recurrent breast carcinoma of the chest wall: Prognostic factors in 196 tumors.,” *International journal of radiation oncology, biology, physics*, vol. 40, no. 2, pp. 365–375, 1998.
- [103] T. Köhler, P. Maass, P. Wust, and M. Seebass, “A fast algorithm to find optimal controls of multiantenna applicators in regional hyperthermia,” *Physics in Medicine & Biology*, vol. 46, no. 9, p. 2503, 2001.
- [104] H. D. Trefná, J. Vrba, and M. Persson, “Time-reversal focusing in microwave hyperthermia for deep-seated tumors,” *Physics in Medicine & Biology*, vol. 55, no. 8, p. 2167, 2010.
- [105] P. T. Nguyen, A. M. Abbosh, and S. Crozier, “3-d focused microwave hyperthermia for breast cancer treatment with experimental validation,” *IEEE Transactions on Antennas and Propagation*, vol. 65, no. 7, pp. 3489–3500, 2017.

-
- [106] D. A. Iero, T. Isernia, A. F. Morabito, I. Catapano, and L. Crocco, "Optimal constrained field focusing for hyperthermia cancer therapy: A feasibility assessment on realistic phantoms," *Progress In Electromagnetics Research*, vol. 102, pp. 125–141, 2010.
- [107] G. G. Bellizzi, T. Drizdal, G. C. van Rhoon, L. Crocco, T. Isernia, and M. M. Paulides, "The potential of constrained sar focusing for hyperthermia treatment planning: Analysis for the head & neck region," *Physics in Medicine & Biology*, vol. 64, no. 1, p. 015 013, 2018.
- [108] A. Kuehne, E. Oberacker, H. Waiczies, and T. Niendorf, "Solving the time-and frequency-multiplexed problem of constrained radiofrequency induced hyperthermia," *Cancers*, vol. 12, no. 5, p. 1072, 2020.
- [109] Z. Rijnen, J. F. Bakker, R. A. Canters, P. Togni, G. M. Verduijn, P. C. Levendag, G. C. Van Rhoon, and M. M. Paulides, "Clinical integration of software tool vedo for adaptive and quantitative application of phased array hyperthermia in the head and neck," *International journal of Hyperthermia*, vol. 29, no. 3, pp. 181–193, 2013.
- [110] J. Robinson and Y. Rahmat-Samii, "Particle swarm optimization in electromagnetics," *IEEE transactions on antennas and propagation*, vol. 52, no. 2, pp. 397–407, 2004.
- [111] H. H. Pennes, "Analysis of tissue and arterial blood temperatures in the resting human forearm," *Journal of applied physiology*, vol. 1, no. 2, pp. 93–122, 1948.
- [112] C. A. Van den Berg, J. B. Van de Kamer, A. A. De Leeuw, C. R. Jeukens, B. W. Raaymakers, M. van Vulpen, and J. J. Lagendijk, "Towards patient specific thermal modelling of the prostate," *Physics in Medicine & Biology*, vol. 51, no. 4, p. 809, 2006.
- [113] H. P. Kok, J. Gellermann, C. A. Van Den Berg, P. R. Stauffer, J. W. Hand, and J. Crezee, "Thermal modelling using discrete vasculature for thermal therapy: A review," *international Journal of Hyperthermia*, vol. 29, no. 4, pp. 336–345, 2013.
- [114] H. Gothäll, "How to use interpolated material data to model irregular geometries," *Comsol Blog*, 2018.

- [115] R. Gaffoglio, G. Vecchi, M. Righero, G. Giordanengo, and M. Zucchi, “Impact of different modeling approaches in field focusing predictions of hyperthermia cancer therapy,” *Skin (wet)*, vol. 1109, pp. 0–681,
- [116] M. Alnæs, J. Blechta, J. Hake, A. Johansson, B. Kehlet, A. Logg, C. Richardson, J. Ring, M. E. Rognes, and G. N. Wells, “The fenics project version 1.5,” *Archive of Numerical Software*, vol. 3, no. 100, 2015.
- [117] J.-M. Jin, *The finite element method in electromagnetics*. John Wiley & Sons, 2015.
- [118] H. P. Langtangen and K.-A. Mardal, *Introduction to numerical methods for variational problems*. Springer Nature, 2019, vol. 21.
- [119] H. P. Langtangen and A. Logg, *Solving PDEs in python: the FEniCS tutorial I*. Springer Nature, 2017.
- [120] C. B. Dracham, A. Shankar, and R. Madan, “Radiation induced secondary malignancies: A review article,” *Radiation oncology journal*, vol. 36, no. 2, p. 85, 2018.
- [121] J. Overgaard, “The heat is (still) on—the past and future of hyperthermic radiation oncology,” *Radiotherapy and Oncology*, vol. 109, no. 2, pp. 185–187, 2013.
- [122] X. Mei, R. Ten Cate, C. M. van Leeuwen, H. M. Rodermond, L. de Leeuw, D. Dimitrakopoulou, L. J. Stalpers, J. Crezee, H. P. Kok, N. A. Franken, *et al.*, “Radiosensitization by hyperthermia: The effects of temperature, sequence, and time interval in cervical cell lines,” *Cancers*, vol. 12, no. 3, p. 582, 2020.
- [123] M. D. Hurwitz, J. L. Hansen, S. Prokopios-Davos, J. Manola, Q. Wang, B. A. Bornstein, K. Hynynen, and I. D. Kaplan, “Hyperthermia combined with radiation for the treatment of locally advanced prostate cancer: Long-term results from dana-farber cancer institute study 94-153,” *Cancer*, vol. 117, no. 3, pp. 510–516, 2011.
- [124] A. Bakker, J. van der Zee, G. van Tienhoven, H. P. Kok, C. R. Rasch, and H. Crezee, “Temperature and thermal dose during radiotherapy and hyperthermia for recurrent breast cancer are related to clinical outcome and thermal toxicity: A systematic review,” *International Journal of Hyperthermia*, vol. 36, no. 1, pp. 1023–1038, 2019.

-
- [125] J. Overgaard, "Simultaneous and sequential hyperthermia and radiation treatment of an experimental tumor and its surrounding normal tissue in vivo," *International Journal of Radiation Oncology* Biology* Physics*, vol. 6, no. 11, pp. 1507–1517, 1980.
- [126] C. M. van Leeuwen, A. L. Oei, K. W. Chin, J. Crezee, A. Bel, A. M. Westermann, M. R. Buist, N. A. Franken, L. J. Stalpers, and H. P. Kok, "A short time interval between radiotherapy and hyperthermia reduces in-field recurrence and mortality in women with advanced cervical cancer," *Radiation Oncology*, vol. 12, no. 1, pp. 1–8, 2017.
- [127] C. Van Leeuwen, J. Crezee, A. Oei, N. Franken, L. Stalpers, A. Bel, and H. Kok, "The effect of time interval between radiotherapy and hyperthermia on planned equivalent radiation dose," *International Journal of Hyperthermia*, vol. 34, no. 7, pp. 901–909, 2018.
- [128] N. R. Datta and S. Bodis, "Hyperthermia with radiotherapy reduces tumour alpha/beta: Insights from trials of thermoradiotherapy vs radiotherapy alone," *Radiotherapy and Oncology*, vol. 138, pp. 1–8, 2019.
- [129] H. Crezee, C. M. van Leeuwen, A. L. Oei, L. J. Stalpers, A. Bel, N. A. Franken, and H. P. Kok, "Thermoradiotherapy planning: Integration in routine clinical practice," *International Journal of Hyperthermia*, vol. 32, no. 1, pp. 41–49, 2016.
- [130] A. M. De Mendoza, S. Michliková, J. Berger, J. Karschau, L. A. Kunz-Schughart, and D. D. McLeod, "Mathematical model for the thermal enhancement of radiation response: Thermodynamic approach," *Scientific Reports*, vol. 11, no. 1, pp. 1–14, 2021.
- [131] M. C. Joiner and A. J. van der Kogel, *Basic clinical radiobiology*. CRC press, 2018.
- [132] L. Bodgi, A. Canet, L. Pujo-Menjouet, A. Lesne, J.-M. Victor, and N. Foray, "Mathematical models of radiation action on living cells: From the target theory to the modern approaches. a historical and critical review," *Journal of theoretical biology*, vol. 394, pp. 93–101, 2016.
- [133] H. Kampinga and E. Dikomey, "Hyperthermic radiosensitization: Mode of action and clinical relevance," *International journal of radiation biology*, vol. 77, no. 4, pp. 399–408, 2001.

- [134] J. R. Lepock, “How do cells respond to their thermal environment?” *International journal of hyperthermia*, vol. 21, no. 8, pp. 681–687, 2005.
- [135] J. L. Roti Roti, “Cellular responses to hyperthermia (40–46 c): Cell killing and molecular events,” *International Journal of hyperthermia*, vol. 24, no. 1, pp. 3–15, 2008.
- [136] S. C. Brüningk, J. Ijaz, I. Rivens, S. Nill, G. Ter Haar, and U. Oelfke, “A comprehensive model for heat-induced radio-sensitisation,” *International Journal of Hyperthermia*, vol. 34, no. 4, pp. 392–402, 2018.
- [137] L. Leksell, “The stereotactic method and radiosurgery of the brain,” *Acta chir scand*, vol. 102, pp. 316–319, 1951.
- [138] V. Svedberg, *Development of a test bench for gamma knife optimization*, 2014.
- [139] C. Lindquist and I. Paddick, “The leksell gamma knife perfexion and comparisons with its predecessors,” *Operative Neurosurgery*, vol. 61, no. suppl_3, ONS–130, 2007.
- [140] J. M. Herman, J. H. Petit, P. Amin, Y. Kwok, P. R. Dutta, and L. S. Chin, “Repeat gamma knife radiosurgery for refractory or recurrent trigeminal neuralgia: Treatment outcomes and quality-of-life assessment,” *International Journal of Radiation Oncology* Biology* Physics*, vol. 59, no. 1, pp. 112–116, 2004.
- [141] A. Donnet, D. Valade, and J. Regis, “Gamma knife treatment for refractory cluster headache: Prospective open trial,” *Journal of Neurology, Neurosurgery & Psychiatry*, vol. 76, no. 2, pp. 218–221, 2005.
- [142] I. Toma-Dasu and A. Dasu, “Modelling tumour oxygenation, reoxygenation and implications on treatment outcome,” *Computational and mathematical methods in medicine*, vol. 2013, 2013.
- [143] C. Van Leeuwen, J. Crezee, A. Oei, N. Franken, L. Stalpers, A. Bel, and H. Kok, “3d radiobiological evaluation of combined radiotherapy and hyperthermia treatments,” *International Journal of Hyperthermia*, vol. 33, no. 2, pp. 160–169, 2017.

-
- [144] C. Van Leeuwen, A. Oei, R. Ten Cate, N. Franken, A. Bel, L. Stalpers, J. Crezee, and H. Kok, "Measurement and analysis of the impact of time-interval, temperature and radiation dose on tumour cell survival and its application in thermoradiotherapy plan evaluation," *International Journal of Hyperthermia*, vol. 34, no. 1, pp. 30–38, 2018.
- [145] J. Van de Kamer, N. Van Wieringen, A. De Leeuw, and J. Lagendijk, "The significance of accurate dielectric tissue data for hyperthermia treatment planning," *International journal of hyperthermia*, vol. 17, no. 2, pp. 123–142, 2001.
- [146] E. Schena, D. Tosi, P. Saccomandi, E. Lewis, and T. Kim, "Fiber optic sensors for temperature monitoring during thermal treatments: An overview," *Sensors*, vol. 16, no. 7, p. 1144, 2016.
- [147] P. Wust, C. H. Cho, B. Hildebrandt, and J. Gellermann, "Thermal monitoring: Invasive, minimal-invasive and non-invasive approaches," *International Journal of Hyperthermia*, vol. 22, no. 3, pp. 255–262, 2006.
- [148] L. Winter, E. Oberacker, K. Paul, Y. Ji, C. Oezerdem, P. Ghadjar, A. Thieme, V. Budach, P. Wust, and T. Niendorf, "Magnetic resonance thermometry: Methodology, pitfalls and practical solutions," *International Journal of Hyperthermia*, vol. 32, no. 1, pp. 63–75, 2016.
- [149] F. Adibzadeh, K. Sumser, S. Curto, D. T. Yeo, A. A. Shishegar, and M. M. Paulides, "Systematic review of pre-clinical and clinical devices for magnetic resonance-guided radiofrequency hyperthermia," *International Journal of Hyperthermia*, vol. 37, no. 1, pp. 15–27, 2020.
- [150] R. M. Arthur, W. Straube, J. Trobaugh, and E. Moros, "Non-invasive estimation of hyperthermia temperatures with ultrasound," *International journal of hyperthermia*, vol. 21, no. 6, pp. 589–600, 2005.
- [151] M.-R. Tofghi and J. R. Pardeshi, "Interference enhanced biomedical antenna for combined heating and radiometry application," *IEEE Antennas and Wireless Propagation Letters*, vol. 16, pp. 1895–1898, 2017.
- [152] E. Groumpas, M. Koutsoupidou, I. S. Karanasiou, C. Papageorgiou, and N. Uzunoglu, "Real-time passive brain monitoring system using near-field microwave radiometry," *IEEE Transactions on Biomedical Engineering*, vol. 67, no. 1, pp. 158–165, 2019.

- [153] M. Haynes, J. Stang, and M. Moghaddam, “Real-time microwave imaging of differential temperature for thermal therapy monitoring,” *IEEE Transactions on Biomedical Engineering*, vol. 61, no. 6, pp. 1787–1797, 2014.
- [154] G. Chen, J. Stang, M. Haynes, E. Leuthardt, and M. Moghaddam, “Real-time three-dimensional microwave monitoring of interstitial thermal therapy,” *IEEE Transactions on Biomedical Engineering*, vol. 65, no. 3, pp. 528–538, 2017.
- [155] G. Chen, M. Moghaddam, J. Stang, and M. Haynes, *Real-time 3d microwave monitoring of thermal therapy*, US Patent App. 16/469,047, Mar. 2020.
- [156] A. Prokhorova, S. Ley, and M. Helbig, “Quantitative interpretation of uwb radar images for non-invasive tissue temperature estimation during hyperthermia,” *Diagnostics*, vol. 11, no. 5, p. 818, 2021.
- [157] S. Ley, S. Schilling, O. Fiser, J. Vrba, J. Sachs, and M. Helbig, “Ultra-wideband temperature dependent dielectric spectroscopy of porcine tissue and blood in the microwave frequency range,” *Sensors*, vol. 19, no. 7, p. 1707, 2019.
- [158] A. N. Tikhonov, A. Goncharsky, V. Stepanov, and A. G. Yagola, *Numerical methods for the solution of ill-posed problems*. Springer Science & Business Media, 2013, vol. 328.
- [159] N. Koshev and L. Beilina, “An adaptive finite element method for fredholm integral equations of the first kind and its verification on experimental data,” *Open Mathematics*, vol. 11, no. 8, pp. 1489–1509, 2013.